

# Coupling Tin-Vacancy Centres to Diamond Waveguides

by

Christian Francesco Primavera

in partial fulfillment of the requirements for the degree of  
Master of Science in Applied Physics at the Delft University of Technology,  
to be presented publicly and defended privately on June 8th, 2022.

Student number: 4586786  
Project duration: September 1, 2021 – May 25, 2022  
Daily supervision: Matteo Pasini MSc TU Delft  
Thesis committee: Prof. dr. ir. Ronald Hanson, TU Delft, supervisor  
Dr. Richard A. Norte, TU Delft  
Dr. Johannes Borregaard, TU Delft

*This thesis is confidential and cannot be made public.*

When released publicly, an electronic version of this thesis will be available at  
<https://repository.tudelft.nl/>.



# Abstract

SnV centres in diamond are a promising candidate for quantum internet applications because of their strong spin-photon interface, long spin coherence times, and insensitivity to electric fields. Integrating them in diamond waveguides could strongly improve entanglement rates and could make for a scalable design. In this thesis, we show using simulations that rectangular  $\langle 110 \rangle$  waveguides are good candidates for high emitter-waveguide coupling, reaching a maximum of 79%. Optimal dimensions are 250 nm x 120 nm (width x height). This also falls inside the single-mode regime for the emitted light. The measured lifetime limits for the linewidth of  $\Gamma = 25$  MHz, dephasing of  $\Gamma_d = 10$  MHz, and  $>10$  seconds long spectral stability in the bulk diamond sample, together with an APD dark count rate of 171 Hz should lead to a transmission dip around resonance of  $\Delta T/T = 25\%$ , which we predict using a different simulation. The currently obtained taper coupling from diamond waveguide to optical fiber is approximately 10%. This is probably enough to see the transmission dip, but it needs to be improved for future experiments. Post-selecting SnV centres in waveguides and using Purcell enhancement to boost ZPL emission can further improve these results.



# Contents

<b>1</b>	<b>Introduction</b>	<b>1</b>
<b>2</b>	<b>Theory</b>	<b>3</b>
2.1	Motivation for Using SnV Centres in Diamond . . . . .	3
2.2	Location of the SnV Centre in the Diamond Crystal . . . . .	3
2.3	Level Structure of the SnV Centre . . . . .	4
2.4	Dipole Emission of the SnV Centre . . . . .	5
2.5	Reshaping the Emission Using Waveguides . . . . .	5
2.6	Taper Coupling Fibers to the Waveguides. . . . .	5
2.7	Waveguides in the Single Mode Regime . . . . .	6
2.8	Dipole Emitter Coupling to Waveguide Modes . . . . .	6
2.9	Purcell Enhancement in Waveguides . . . . .	7
2.10	Non-Linear Response of Waveguide-Emitter System . . . . .	7
<b>3</b>	<b>Waveguide Coupling Simulations</b>	<b>9</b>
3.1	Fabrication Process and its Implications for the Geometry. . . . .	9
3.2	Simulations for Finding the Single Mode Regime. . . . .	10
3.3	Different Orientations of the Waveguides . . . . .	11
3.4	Simulations for Optimizing the Emitter-Waveguide Coupling. . . . .	11
3.5	Simulating an Offset of the Dipole . . . . .	12
3.6	Waveguides in $\langle 111 \rangle$ Samples . . . . .	13
3.7	Simulations for Purcell Enhancement . . . . .	14
3.8	Conclusions for Optimal Waveguide Design . . . . .	15
<b>4</b>	<b>Experimental Determination of Parameters</b>	<b>17</b>
4.1	Optical Transition Decay Rate . . . . .	18
4.2	Spectral Stability . . . . .	19
4.3	Pure Optical Dephasing Rate . . . . .	20
4.4	Taper Coupling . . . . .	22
4.5	Experimental Setup . . . . .	27
4.6	APD Dark Count Rate . . . . .	28
<b>5</b>	<b>Transmission Dip Simulations</b>	<b>29</b>
5.1	Transmission Dip as a Function of Laser Power . . . . .	29
5.2	Improvement of Waveguide-Emitter Coupling. . . . .	30
5.3	Improved Taper Coupling . . . . .	31
5.4	Repeated Measurements . . . . .	31
<b>6</b>	<b>Conclusion &amp; Outlook</b>	<b>33</b>
<b>A</b>	<b>Waveguide Simulations Methods and Settings</b>	<b>35</b>
A.1	Finding the Single Mode Regime . . . . .	35
A.2	Finding the Coupling Factors for the Waveguides . . . . .	36
<b>B</b>	<b>Supporting Information Experiments</b>	<b>39</b>
B.1	Optical Transition Decay Rate . . . . .	39
B.2	Pure Optical Dephasing Rate . . . . .	40
B.3	Saturation Power . . . . .	40
<b>C</b>	<b>Transmission Dip Simulations</b>	<b>41</b>



# 1

## Introduction

### **A Potential Building Block for the Quantum Internet**

At its birth early in the 20th century, the theory of quantum mechanics was proposed to describe the behaviour of nature on the smallest scale known. Later during the 20th century, the idea arose to develop technology based on building up large systems of particles which still shows this ‘quantum behaviour’. One of the applications the scientific community is working towards is the quantum internet, enabling fundamentally secure communication, remote access to future quantum computers, distributed quantum computing, and possibly various applications still unknown [25].

A reliable quantum internet requires its constituent quantum bits to fulfill certain criteria, proposed by David DiVincenzo in 2000 [6]. In addition to the requirements for quantum computation, quantum communication requires a strong interface between stationary and flying qubits and a way to faithfully transmit the flying qubits from one place to another. Photons seem apt for the role of flying qubits. This has drawn attention to color centres in diamond because of their efficient spin-photon interface.

Negatively charged tin-vacancy centres are promising candidates for use in a quantum internet because of their large orbital splitting [11], which reduces the effect of a decoherence mechanism that plays an important role in other color centres at low temperature. Furthermore, their high quantum efficiency [12] and Debye-Waller factor [9] promise high entanglement rates. Lastly, their insensitivity to fluctuating electric fields arising from the centrosymmetric defect structure gives us the possibility of integrating them in nanophotonic devices which can increase entanglement rates even further and at the same time make the system scalable [19, 24].

For the future quantum internet, we would need the possibility to mass-produce the structures in which the qubits are located, and the ability to integrate them on a platform to access them individually such as a photonic integrated circuit. A step towards this goal is embedding negatively charged tin-vacancy centres in diamond waveguides, which is the subject of this project.

### **Project Goal**

This project works towards a better understanding of tin-vacancy centres in diamond waveguides. The original goal of the project was to measure optical non-linear behaviour of a tin-vacancy centre in a waveguide, accessed by optical fibers. In the end, the sample on which we plan to measure this was delayed. We do have a sample with ‘empty’ waveguides (without tin-vacancies) and a ‘bulk’ diamond sample with tin-vacancies (that is, without waveguides). The thesis is therefore structured as follows:

### **Thesis Structure**

The first part of the project focuses on the requirements for the waveguides that I determined from simulations (Chapter 3). The second part aims to measure characteristics of our experimental setup and of the tin-vacancy centres in bulk diamond (Chapter 4). The third part is a simulation for if and how strongly we expect to measure an optical non-linearity created by the emitter-waveguide system (Chapter 5).

## Personal Contribution

The theory in this thesis (Chapter 2) results from a literature study. The simulations (Chapters 3 & 5) are my own work. I carried out most of the experimental measurements and data analysis (Chapter 4). The measurement and analysis scripts for the SnV centre measurements have been written by previous researchers, I only modified them to better fit these specific measurements. I worked with Matteo Pasini on the design of the experimental setup used for fiber coupling, designing the inside of the cryostat is his work. The waveguide samples were fabricated by Nina Codreanu.

## Acknowledgements

Research in experimental physics is generally not done alone. Throughout this project I have seen the team effort required to find out more about the behaviour of the world around us. I appreciated the attention in the department for getting to know one another. Social events like the QuTech 'Uitje', having dinner together, or celebrations of milestones are not only fun, but really helped finding the right people to contact later when needed.

First and foremost, I would like to thank Matteo. I was the first master student under your supervision, but this has not been apparent in any way. Your feedback was predominantly positive, but you have also not missed a single opportunity to give me points for improvement, which has really helped me throughout the project. Every time I was disappointed with the practical progress in the lab, I had completely new energy after one of our meetings. You have shown you're not only concerned with your own work, but also what other people are up to. You are a driving force of the good ambiance in the group and in general very fun to be around. You're passionate to reach your goals, and you have the ability to find creative solutions when things don't go according to plan. I wish you the best of luck with finishing your PhD and whatever may come after!

Ronald, what really surprised me from the beginning was your signal-to-noise ratio when speaking: the care with which you choose your words is unparalleled. More seriously, I think your leadership style is admirable. You are able to give loads of freedom and responsibility to each person in the group, while at the same time inspiring everyone to work on the research with great enthusiasm and dedication. Thank you for this opportunity!

The SnV meetings were an example to me of how discussions can lead to new ideas for improved models, designs, and measurement plans. Thank you Nina for your passionate presentations about fabrication and your extensive knowledge about plasma etching recipes and high-temperature tri-acid cleaning. I hope you will keep enjoying the cleanroom time as much as you do now! Julia, your positive influence on the group is amazing! The goals for your PhD are ambitious, but your perseverance and can-do mentality will no doubt get you a long way! Hans, I really enjoyed how you always seem to be in a good mood, and I think your intellect proves that nobody is more deserving of becoming two types of doctor at the same time! Christopher, you started your PhD when I had already joined the group, and I've already seen you design an entire experimental setup from scratch. I think your progress is very promising for the next three years! Thank you Lorenzo for the experience you bring to the table. Sometimes only a short comment by you finished the entire discussion, even when it had to come from the other side of the world over zoom. Slava, Johannes, and Fengelei, thank you for all the theoretical contributions on the SnV centres. Sarel, Sezer, Otmar, Rick, Laurens, Margriet, Lisa, Janice, Tijmen, Thomas, Gerben, Lars, and Douwe, I definitely enjoyed our laughs in the master room and the numerous coffees in the pantry.

Finally, I would like to thank all members of the committee in advance for taking the time to read this report, and for taking part in the defence discussion and assessment.

# 2

## Theory

### 2.1. Motivation for Using SnV Centres in Diamond

Group IV color centres in diamond, like the SiV, GeV, SnV, and PbV have a strong spin-photon interface [17]. Of these group IV centres, the negatively charged tin vacancy (SnV<sup>-</sup>) centre is very promising. It has a high quantum efficiency (~80%) [12] and high Debye-Waller factor (~60%) [9]. The fact that the SnV has a larger orbital splitting of the ground state than other group IV color centres [4], suggests that SnV centres might be less affected by phonon-induced orbital relaxations, resulting in longer spin coherence times around 1K [12]. These factors result in fast generation and long retention of entanglement, making the SnV centre a good candidate for a next generation of qubits for quantum networks.

Another advantage of SnV centres is their first-order insensitivity to fluctuating electric fields [20], arising from their predicted electronic structure [11] because of the  $D_{3d}$  symmetry of the defect (see figure 2.1). This makes them suitable for use in nanophotonic waveguides and cavities [2], improving the spin-photon interface by way of a strong coupling of the photonic mode in the waveguide to the dipole. This promises higher entanglement rates in future quantum networks and could improve the scalability of the system [24]. It is therefore interesting to investigate how exactly we should integrate SnV centres in waveguides and what coupling we can achieve.

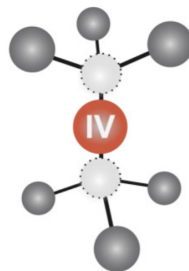


Figure 2.1: Defect structure of group IV vacancy centres in diamond. Adapted from [17].

### 2.2. Location of the SnV Centre in the Diamond Crystal

The diamond crystal structure is composed of regular repetitions of the unit cell shown in figure 2.2. All black balls are carbon atoms, forming two FCC lattices, one offset  $(\frac{1}{4}, \frac{1}{4}, \frac{1}{4})$  from the other. The crystallographic directions  $\langle 100 \rangle$ ,  $\langle 110 \rangle$  and  $\langle 111 \rangle$  have been visualised. Note that there are many directions which are equivalent to these because of the symmetries of the arrangement. The carbon-carbon bonds all coincide with a  $\langle 111 \rangle$  direction. Since the Sn atom sits at the interstitial position between two neighbouring carbon atoms, the symmetry axis of the defect is always in one of the  $\langle 111 \rangle$  directions.

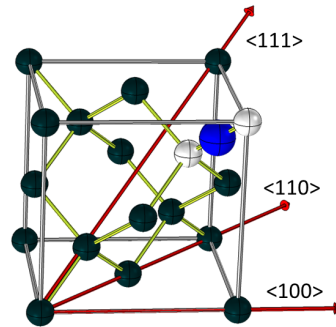


Figure 2.2: Ball-and-stick model of a unit cell of the diamond crystal structure, with one SnV centre in it. The black balls are carbon atoms, the white balls indicate where two carbon atoms are missing. The blue ball is a tin atom. Three important directions that will be used in this thesis are indicated with red arrows.

### 2.3. Level Structure of the SnV Centre

The SnV centre has many of the same properties of a different group IV color centre which about which more is known, the SiV (silicon-vacancy) centre. Both defects consist of the group IV atom at the interstitial position of two missing carbon atoms, and the electronic structure is formed by 6 electrons from the dangling bonds in addition to 4 from the group IV atom and one free electron which is captured. For the SiV centre, Hepp calculated the electronic structure from symmetry groups using group theory [11]. Currently, the theoretical model for the SnV centre is being revised, but Hepp's model of the SiV centre suffices for the purposes of this thesis.

The level structure resulting from this model is shown in figure 2.3. Both the ground state and excited state are four-fold degenerate. At  $B=0$ , both states are split by a combination of spin-orbit interaction and the Jahn-Teller effect. If a magnetic field is present, the spin up and down states will be split by the Zeeman effect. We are planning to use the two spin states of the lower orbital branch of the ground state as the two qubit levels (dashed box in the figure). Microwave driving between these two levels is not yet possible, as this transition requires flipping both the spin and the orbital state. Straining the diamond mixes up the spin states slightly more and might lead to functioning microwave driving of this transition in the future.

The transition between the ground state and excited state which will be mentioned often in this thesis is indicated in red. This transition of 2.0eV corresponds to a photon with free-space wavelength of approximately 619nm. It will be used to excite the SnV centre and will be what the SnV centre mostly emits in the zero-phonon line.

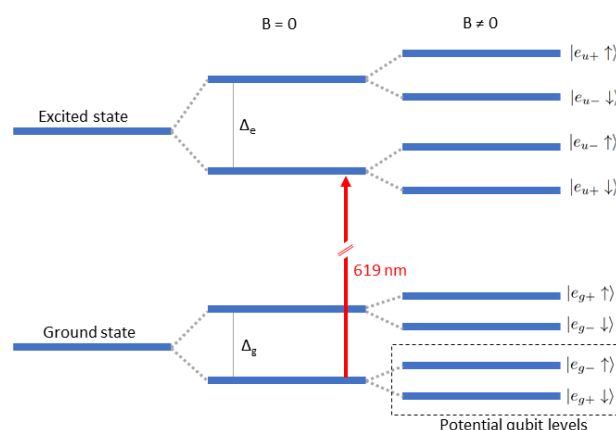


Figure 2.3: Model for the level structure of SnV<sup>-</sup> centres. It shows the splitting of the excited state and the ground state, first at  $B=0$  by a combination of spin-orbit coupling and the Jahn-Teller effect, and then at  $B\neq 0$  by the Zeeman splitting. The levels that we plan on using as a qubit in future experiments are indicated in the dashed box. It also indicates the transition corresponding to a photon with 619nm free-space wavelength.

## 2.4. Dipole Emission of the SnV Centre

Calculating the emission pattern of the transition between two atomic states can be done using a hybrid quantum-classical approach. In this approach, we are looking for the interaction between the emitter which we treat quantum mechanically and the electro-magnetic field, which we treat classically.

The classical electro-magnetic field is described by the Maxwell equations. To obtain a particularly useful description of the interaction, we use a derivation explained in [10], in which the Göppert-Mayer gauge is chosen. This results in the following Hamiltonian:

$$\hat{H} = \frac{\hat{\mathbf{p}}^2}{2m} + V_{\text{Coul}}(\hat{\mathbf{r}}) - \hat{\mathbf{D}} \cdot \mathbf{E}(\mathbf{r}_0, t). \quad (2.1)$$

This Hamiltonian is nothing more than a standard Coulomb Hamiltonian with an interaction term added of an electric dipole interacting with the electric field. This result is useful, because it allows for a simple way of modeling the emission pattern of our SnV centres. We can just use classical EM finite element simulations to find the emission pattern of a dipole emitter to determine the coupling of the centre to a waveguide.

## 2.5. Reshaping the Emission Using Waveguides

The standard free-space emission pattern of a dipole is not ideal for a high photon collection efficiency, since the radiation intensity does not depend on the azimuth. Dipoles therefore emit in many directions, but changing the dielectric environment of the emitter can reshape its emission pattern. In our case, we try to do this using a waveguide. The waveguides we use are long thin beams made of a material with a higher refractive index than the surrounding material, shown in figure 2.4a. The diamond in which the SnV centre is located ( $n \approx 2.4$ ) serves as an excellent material. When surrounded by air or vacuum ( $n \approx 1$ ) this is expected to display clear waveguiding properties.

We expect the waveguide to reshape the emission pattern such that most of the radiation will be emitted inside the waveguide. The effect is visualised in figure 2.4b, which shows one of the simulations that are discussed in the next chapter. From the figure it is clear that most light stays inside the waveguide, and I will quantify this effect later on.

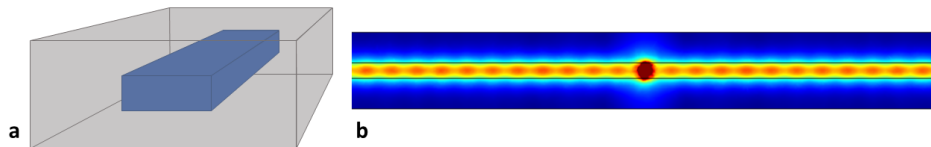


Figure 2.4: Typical result of dipole emission in a waveguide. (a) shows the the waveguide geometry and the surrounding volume of vacuum. The waveguide is just a diamond cuboid. (b) shows the electric field norm on a slice through the waveguide. It is clear that most of the radiation stays inside the waveguide. How much exactly will be quantified later. Simulated using COMSOL Multiphysics.

## 2.6. Taper Coupling Fibers to the Waveguides

The light emitted into the waveguide can then be coupled into optical fibers by what is called a tapered coupling. The ends of both the waveguide and the fiber are tapered at a very sharp angle, such that the mode will transfer into the evanescent field as we move to the tip of the structures. If we bring these together very closely, the two evanescent fields will couple and a shared mode comes into existence, which adiabatically changes from the waveguide mode to the fiber mode in the space domain. A more in depth analysis of this phenomenon (including experiments) is made in [5].



Figure 2.5: Taper coupling between optical fiber and waveguide.

## 2.7. Waveguides in the Single Mode Regime

It is possible to calculate certain modes of the EM waves inside the waveguides. Each mode can carry part of the radiated emission. Emission into multiple modes can make photons distinguishable, will lead to deterioration of the collection efficiency, and scrambles the phase of emitted photons. Therefore, we need to make sure we allow only a single mode in the waveguide. After this, we can optimise the coupling of the emitter to this mode.

Whether a waveguide allows multiple modes or only one is determined by multiple characteristics. Clearly the geometry of the waveguide cross-section plays a role. The shape and size of the cross-section determine which modes ‘fit inside’ for a certain frequency. The ratio between the refractive indices also has an influence. An illustration of different possible modes is shown in figure 2.6.

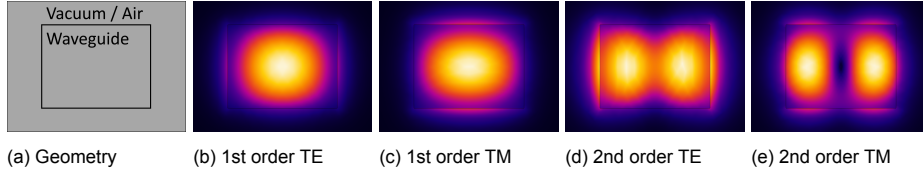


Figure 2.6: Modes of a waveguide of 460nm x 350nm. (a) shows the geometry of the waveguide and the surrounding vacuum or air. The other four images show the electric field norm in a cross-section of the waveguide and the area around it. We see that the mode is not located fully inside the waveguide. Free-space wavelength of light is 620nm.

We will use 2D FDTD simulations using COMSOL Multiphysics to find all possible modes for different parameter values, in order to determine when the waveguides are in the single-mode regime. Because of the numerical approach, we are free to choose shapes that are relevant for the fabrication methods that we will use later on. The results of the simulations, together with the known inaccuracies resulting from fabrication, will be used to find optimal parameters for fabricating the waveguides for the experiments.

## 2.8. Dipole Emitter Coupling to Waveguide Modes

Once we establish the requirements for a single-mode waveguide, we should make sure that it optimally couples to the emitted light in order to maximize the photon collection efficiency. We define the coupling by the factor  $\beta = P_{wg}/P_{total}$ , the ratio between the power emitted into the waveguide mode and the total emitted power.

A practical way of calculating the radiated power by a dipole in a dielectric environment is by calculating the work it exerts on the electric field. The power of a current dipole on the electric field [15] is

$$P_E = -\frac{1}{2}\Re(\mathbf{j} \cdot \mathbf{E}) \quad (2.2)$$

Here, the current dipole

$$\mathbf{j} = \frac{\partial}{\partial t}\mathbf{p} = \frac{\partial}{\partial t}(\mathbf{p}_0 e^{-i\omega t}) = -i\omega\mathbf{p}_0 e^{-i\omega t} = -i\omega\mathbf{p} \quad (2.3)$$

where  $\mathbf{p}$  is the charge dipole moment. From this, we get

$$P_E = -\frac{1}{2}\Re(-i\omega\mathbf{p} \cdot \mathbf{E}) = \frac{\omega}{2}\Im(\mathbf{p} \cdot \mathbf{E}) \quad (2.4)$$

With this result, we can calculate our coupling factor with

$$\beta = \frac{P_{wg}}{P_{total}} = \frac{\Im(E_{\hat{p}}(\mathbf{r}_{far}))}{\Im(E_{\hat{p}}(\mathbf{r}_0))}. \quad (2.5)$$

Where  $E_{\hat{p}}$  is the electric field component in the direction of the dipole. In order to calculate the coupling, we therefore only have to evaluate the electric field in the direction of the dipole resulting from the simulation in two locations: the location of the dipole itself, and a location far away in the waveguide. The location of  $\mathbf{r}_{far}$  is the same as the dipole in the cross-section of the waveguide, but moved a long distance ( $> 5$  wavelengths) away in the propagation direction [16]. How this is done in practice is explained in section 3.4.

## 2.9. Purcell Enhancement in Waveguides

Embedding the dipole in a nanophotonic structure not only affects the coupling to certain photonic modes, but it can also change the total emission rate. The waveguide acts as a very weak cavity, meaning we have to take some Purcell enhancement into account. This can be expressed as the ratio between the power emitted by the dipole in the waveguide, compared to the power that the same dipole would emit in a homogeneous medium. Similar to the situation before, we can express this as [21]

$$F_P = \frac{P_{WG}}{P_{Hom}} = \frac{\Im(E_{\vec{p}}^{WG}(\mathbf{r}_0))}{\Im(E_{\vec{p}}^{Hom}(\mathbf{r}_0))} \quad (2.6)$$

## 2.10. Non-Linear Response of Waveguide-Emitter System

Waveguides not only allow for enhanced collection efficiencies which would improve entanglement schemes based on spin-selective excitation, but also open up the possibility for coherent interaction between the emitter and photons. SnV centres in the waveguides will interact with photons resonant with the optical transition. This interaction has been described in [1]. In the case of a waveguide containing a two level system, this results in reflection of resonant photons sent through the waveguide, which has been worked out in [14, 21]. This effect shows up as a Lorentzian dip around the resonance frequency in the transmitted light through the waveguide, as shown in figure 2.7. The transmission factor on resonance (deepest point of the dip) is then calculated to be

$$T = 1 - \frac{\beta(2 - \beta)}{(1 + 2\Gamma_d/\Gamma)(1 + n_\tau/n_c)} \quad (2.7)$$

where  $\beta$  is the coupling of the emitter to the waveguide mode, which we determine with simulations in 3.4. This  $\beta$  depends on the waveguide geometry, the dipole orientation, and the dipole location in the waveguide. On top of this,  $\beta$  accounts for the quantum efficiency and the Debye-Waller factor of the defect. Furthermore,  $\Gamma_d$  is the pure dephasing rate,  $\Gamma$  is the optical decay rate, taking into account the Purcell enhancement.  $n_\tau$  is the mean photon number in the input field within one lifetime of the emitter, and  $n_c$  is the critical photon number given by

$$n_c = \frac{1 + 2\Gamma_d/\Gamma}{4\beta^2} \quad (2.8)$$

$n_\tau/n_c$  is therefore a measure for the saturation of the defect. These parameters not only change the depth of the dip, but also its width. The width (FWHM) is  $(\Gamma + 2\Gamma_d)\sqrt{1 + n_\tau/n_c}$ . This means that dephasing with make the dip wider and more shallow. Increasing the input power towards or past the critical power has the same effect. Lastly, imperfect coupling to the waveguide mode ( $\beta < 1$ ) will also make the dip more shallow, but might also decrease the width slightly. All these effects are visualised in figure 2.7. Keeping below saturation of the defect leads to the requirement of low laser power, but this will also decrease our signal-to-noise ratio. I will therefore simulate the transmission dip we expect for different input powers in Chapter 5.

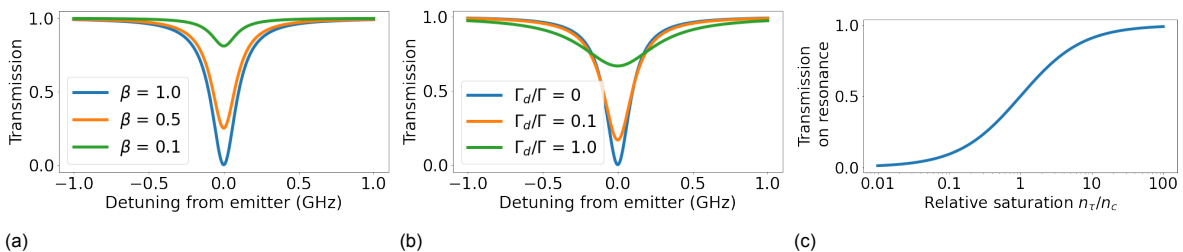


Figure 2.7: (a) Transmission dip for different coupling factors. Strong coupling increases the depth of the dip. (b) Transmission dip for different dephasing rates. More dephasing decreases the depth of the dip and makes it wider. (c) Transmission dip at 0 detuning for different input powers. More power saturates the emitter and makes the dip less deep.



# 3

## Waveguide Coupling Simulations

The simulations are designed such that we can extract optimal fabrication parameters. As became clear from the theory section, we are looking for waveguides that allow only a single mode to propagate and that maximize the coupling to this mode. We will run these simulations separately.

### 3.1. Fabrication Process and its Implications for the Geometry

The fabrication process consists of multiple steps and these can be done in different ways. A possibility for the implantation is to use shallow ion implantation and growth (SIIG), in which the Sn ions are implanted at low energy, followed by a CVD overgrowth of the diamond to tune the depth of the resulting SnV centres. At the moment of writing, we have not yet succeeded at this for  $\langle 100 \rangle$  diamonds. We will therefore start by using high energy implantation (HEI), in which the depth of the Sn ions is controlled up to a certain precision by the amount of energy carried by the ions. Annealing is then used to combine the ions with vacancy centers and partially heal the damage to the crystal caused by implantation.

After the implantation, the waveguides must be etched. The shape of the waveguide will be etched anisotropically from the top, deeper than the actual waveguide needs to be. Then a quasi-isotropic etch is used to release the waveguide from the bulk. This process does leave an uncertainty in the final bottom shape of the waveguide since it can leave slanted edges at an unknown angle, which I will include in the simulation. The fabrication process [18] and resulting geometry are shown in figure 3.1.

The process also allows us to tune the width and height of the waveguide and the depth of the defect. Each of these parameters comes with its own uncertainty. There are also uncertainties arising from other imperfections in the process. There is some variance in the location of the defects, and there might be multiple defects in a single waveguide. In the simulations the waveguide width, height, and bottom angle will be varied, along with the location of the defect within the waveguide.

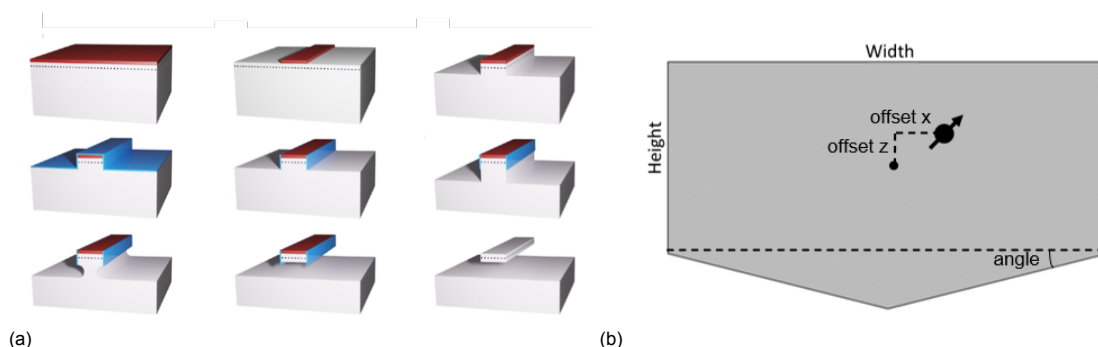


Figure 3.1: Waveguide fabrication process and resulting geometry. (a) shows the fabrication process, consisting of the anisotropic and quasi-isotropic etches, adapted from [18]. (b) shows the resulting cross-section of the waveguide and the location of the defect (black ball with arrow). It also indicates the relevant parameters.

### 3.2. Simulations for Finding the Single Mode Regime

First, we want to make sure the waveguides only allow one mode as argued in section 2.7. First, the width and height are swept for the rectangular waveguide (angle = 0). The results of this sweep are visualized in figure 3.2. In general, higher order modes do not ‘fit’ inside the waveguide as well as the first order modes, pushing them into the air. This means that their effective refractive index is lower. Because of this, the transition between the single-mode and multi-mode regime is very clear from looking at the smallest refractive mode index. Note that a higher effective refractive index does not mean that the coupling will also be larger. Conclusions about the coupling can only be drawn from the second simulation.

We then turn to finding out how the angling on the bottom affects the transition into the multi-mode regime. We simulate the region which has been shown in figure 3.2 for 0°, 15°, 30°, and 45°. The results have been shown in the inset.

From the figure we can find an upper bound for how large the waveguides are allowed to be. We must make sure that, considering the uncertainties in fabrication, the waveguide is no larger than the transition to the multi-mode regime. We now also know how uncertainties in the bottom angle will impact the transition from single-mode to multi-mode regime.

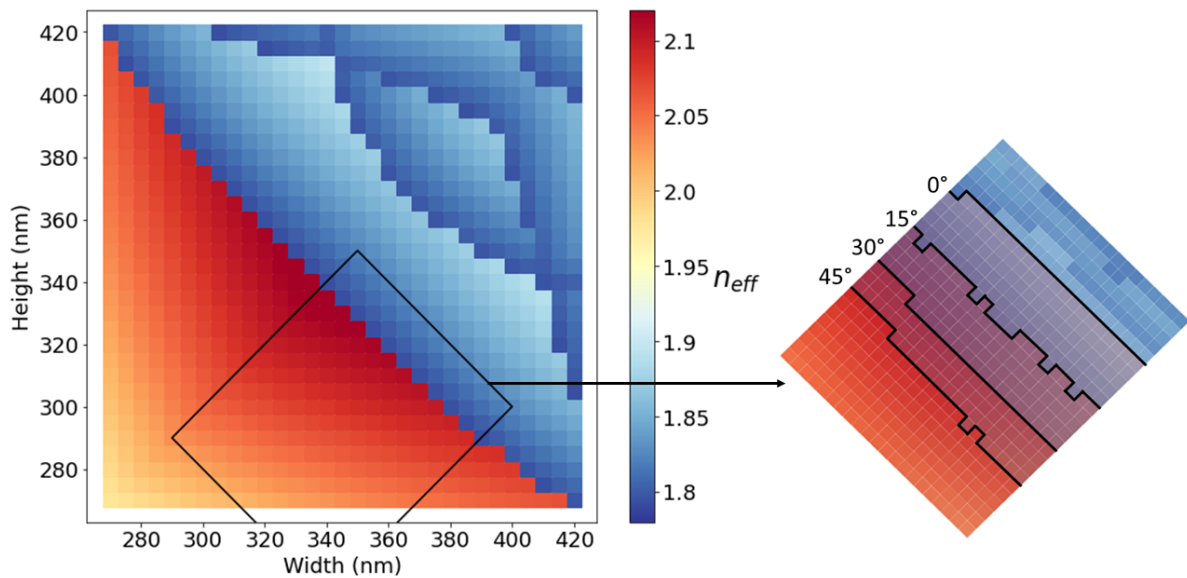


Figure 3.2: The smallest effective refractive indices for different combinations of width and height of a rectangular waveguide. The minimum refractive indices show very clearly where the transition between the single-mode and multi-mode regime is (transition from red to blue). The black rectangle indicates the area shown in the inset, which shows the effect of the different angles. Figures for bottom angles of 0°, 15°, 30°, and 45° have been overlaid and the transitions to the multi-mode regime are indicated for each angle. The original figures with data for different angles can be found in appendix A.

### 3.3. Different Orientations of the Waveguides

While the directions of the dipole emitters with respect to the crystal lattice are fixed, the waveguides can have different orientations. However, the possible directions are restricted by the stability of the lattice planes. We know that the fabrication process works well for at least two different waveguide directions,  $\langle 100 \rangle$  and  $\langle 110 \rangle$ . These directions have been indicated in figure 2.2, and figure 3.3 shows these directions relative to the bulk diamond (in top view) and to the dipole direction.

The figure illustrates that the  $\langle 100 \rangle$  waveguides have a component of the dipole in the direction of the waveguide, while the  $\langle 110 \rangle$  waveguides do not. If we look at the two components of the dipole in the rectangular cross-section of the waveguide (perpendicular to the waveguide direction), we can see the dipoles in the  $\langle 100 \rangle$  waveguides have a component of  $\sqrt{1/3}$  in each of the directions. For the  $\langle 110 \rangle$  waveguides, this is  $\sqrt{2/3}$  and  $\sqrt{1/3}$ . Intuitively, we therefore expect the dipoles to couple more strongly to the  $\langle 110 \rangle$  waveguide modes. I have done simulations for both directions.

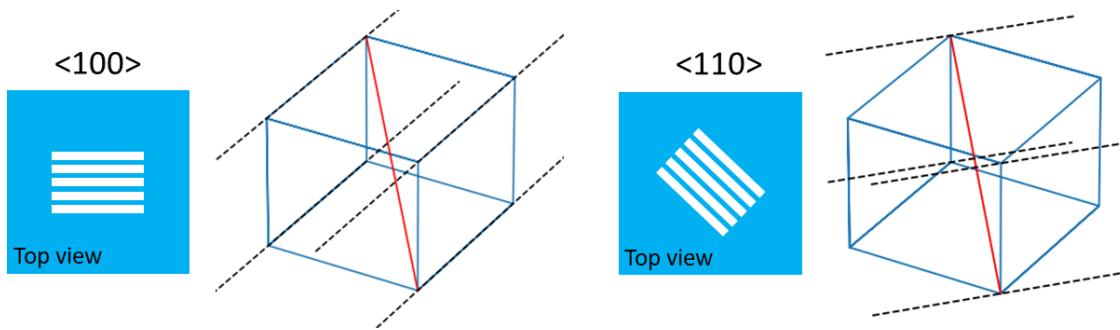


Figure 3.3: Different ways of etching the waveguides. The left and right show  $\langle 100 \rangle$  and  $\langle 110 \rangle$  waveguides respectively. The red lines indicate the dipole direction, the black dashed lines indicate the direction of the waveguide.

### 3.4. Simulations for Optimizing the Emitter-Waveguide Coupling

Having waveguides in the single mode regime makes sure that we can get coherence of the emitted photons, but it does not give information about how we can get the optimal coupling. For this, we can use the calculation made in section 2.8. From equation 2.5, we can tell that the important values of the electric field are located at  $\mathbf{r}_0$  and  $\mathbf{r}_{\text{far}}$ . However, we can not just take any point for  $\mathbf{r}_{\text{far}}$ . Figure 3.4 shows the electric field in the direction of the dipole. We can take the amplitude of the wave and compare it to the electric field at the dipole location to find the coupling. This is similar to the methods used to calculate the coupling in [21] and [16].

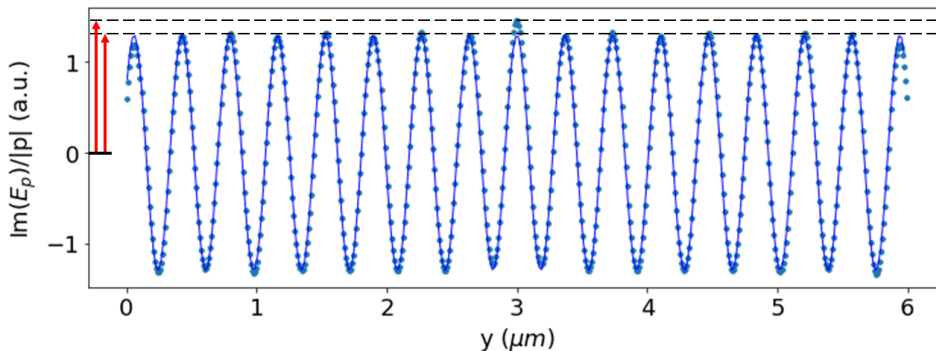


Figure 3.4: Imaginary part of the electric field in the direction of the dipole, generated by the emitter, normalized by the strength of the dipole. On the horizontal axis ( $y$ ) is the distance in the direction of the waveguide. Scattered points indicate the result from the simulation. The blue line is a fit. In this case, the dipole was oriented in the  $x$ -direction, so only the TE mode was excited, and the fit indicates a single cosine wave. We see that the E-field deviates from the fit at the location of the emitter, and transitions to the cosine wave (the mode in the waveguide) when moving further away from the defect. Dashed lines indicate the amplitude at  $\mathbf{r}_0$  and in the far field. The ratio between the amplitudes (the lengths of the two red arrows) yields the coupling factor, which in the case of this figure is 87%.

In general, the waveguides in the single-mode regime allow both a TE and a TM mode, which can have different wavelengths (since they can have different effective refractive indices). The electric field is therefore fit to a sum of two cosine functions. The plot in figure 3.4 is a special case where the dipole was pointed in the x direction, leading to the excitation of only the TE mode. For the experiments, we are interested in achieving an optimal coupling to only one of the modes. The value plotted in the rest of the results is therefore always the maximum of the two amplitudes, not the sum. The other light will also go through the waveguide, but will not be of use for anything which requires indistinguishability or coherence of the light.

In order to find the optimal size of the waveguide, the width and height of the waveguides are swept. The resulting coupling factors for both waveguide orientations are shown in figure 3.5. There is an optimum in waveguide size for getting a maximum coupling, and the  $\langle 110 \rangle$  waveguides clearly outperform the  $\langle 100 \rangle$  waveguides. This is consistent with our expectations since the dipole has a larger component in the direction of the electric field of the mode.

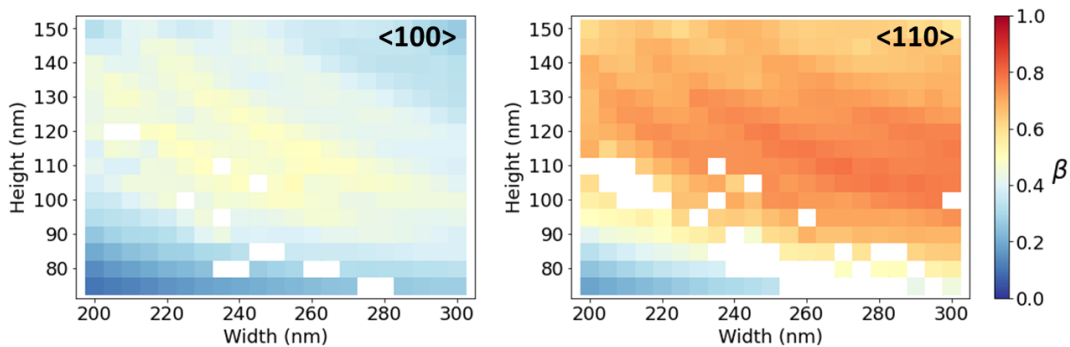


Figure 3.5: Coupling factors  $\beta$  between dipole and waveguide.  $\langle 100 \rangle$  and  $\langle 110 \rangle$  waveguides are shown separately. Both figures contain values for various sizes of the waveguides, with the dipole located exactly in the middle. The figure shows some missing values, resulting from curve fitting which was not accurate enough. More information about the calculation is in the appendix. The maximum couplings obtained are 50% and 79%, for  $\langle 100 \rangle$  and  $\langle 110 \rangle$  waveguides respectively. The 79% is not too far off from the maximum estimated in [23], which is 81%. The area shown is already an optimised regime, a broader scan can be found in the appendix.

### 3.5. Simulating an Offset of the Dipole

We don't have full control over the exact location of the defect, so I simulated the effects of an offset in the x and z direction (the directions in the cross-section of the waveguide). The waveguide size will now be fixed to 250nm x 120nm and the location of the dipole will be varied. The results are shown in figure 3.6. From the figures, it can be seen that the  $\langle 110 \rangle$  outperforms the  $\langle 100 \rangle$  waveguides in most locations. It is also clear that the coupling does not drop off dramatically for most of the waveguide in the  $\langle 110 \rangle$  direction, only at the edge.

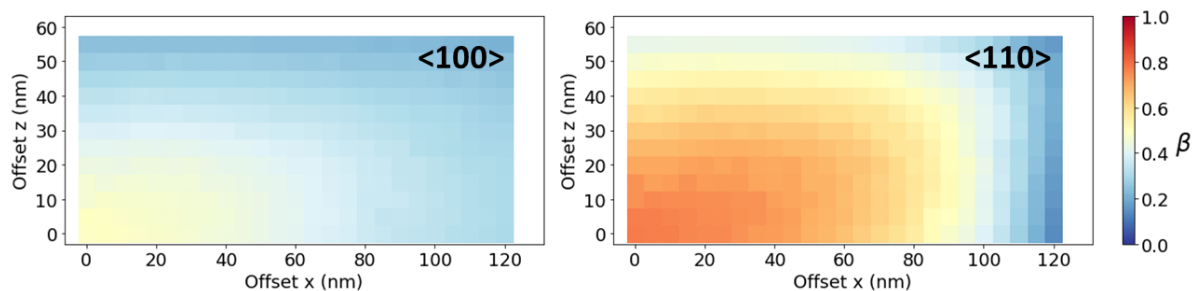


Figure 3.6: Coupling factors  $\beta$  between dipole and waveguide. Figures show the  $\langle 100 \rangle$  and the  $\langle 110 \rangle$  waveguides. Both figures contain values for various locations of the dipole within the waveguide (bottom left is the centre), while the waveguide size is fixed to 250 nm x 120 nm. For  $\langle 100 \rangle$ , the coupling in the centre is 49.18%, which drops to 30.30% and 24.26% in the x and z directions respectively, when getting all the way to the edge of the waveguide. For  $\langle 110 \rangle$ , the centre is 77.24%, dropping of to 14.39% and 42.81%.

### 3.6. Waveguides in <111> Samples

All the waveguides considered in this thesis concern those fabricated in <100> grown diamond samples. Another possibility would be to use a sample that has been overgrown in the <111> direction. In that case, we could create waveguides in the plane which have 1 in 4 dipoles oriented in a very advantageous way. Figure 3.7 shows the results for this simulation. It can be seen that the optimal regime here is where the waveguides are higher and more narrow.

The figure shows that the <111> waveguides can reach coupling factors of up to 89% which is really impressive, and an improvement over the <110> waveguides. However, the waveguide fabrication recipe we use relies on etching along definite crystallographic planes to suspend the structures. It is unclear whether this recipe would work on <111> oriented samples.

The fact that our current process would not work is not in itself a good reason to not do it, but the problem is not just that it would take more work. In the <111> samples, we would need to either come up with a differently shaped waveguide (for which it is still uncertain how good the coupling factors will be), or the waveguides will turn out with a high amount of imperfections and surface roughness (which likely also impacts the coupling efficiency). For these reasons, I decided not to further investigate this type of waveguides, in consultation with people working on fabrication.

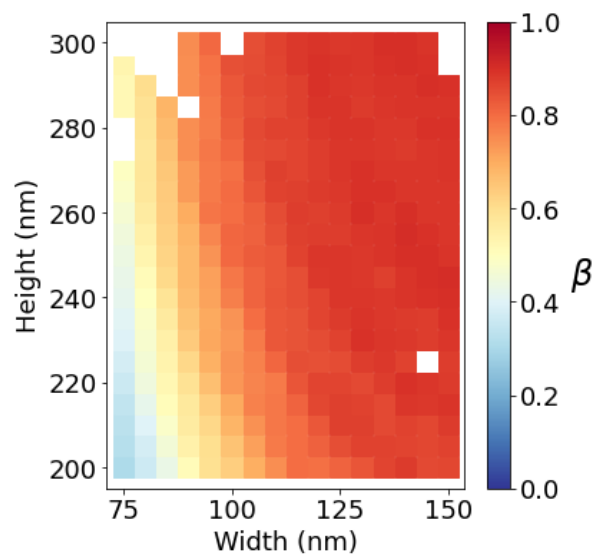


Figure 3.7: Simulated coupling factors for waveguides in <111> samples. Maximum coupling reached is 89%.

### 3.7. Simulations for Purcell Enhancement

The previous simulations have made clear that the regime for optimal coupling is reached for waveguides in the  $\langle 110 \rangle$  direction, and for widths between 200-300nm, and heights between 75-150nm. For these values, I have simulated the Purcell enhancement. Based on equation 2.6, I do this by simulating the situation of the dipole in the waveguide, and comparing this to the situation where the same dipole is located in a homogeneous medium. The ratio of the E-field values in the direction of the dipole on the location of the dipole gives the Purcell factor. The results are shown in figure 3.8. This is done for various waveguide sizes and dipole offsets.

Figure 3.8 shows that the Purcell factor varies from 1.75 to 2.5 throughout the regime. It also seems to be quite sensitive to small changes in dimensions. These changes are arguably too small to take into account during fabrication. Since the coupling is also a more important figure of merit for the waveguides, we will not optimise the design for a high Purcell factor. However, it is important to know that the Purcell factor is not negligible and that we have to take it into account when doing further simulations and analysis of our experiments.

The figure on the right shows that the Purcell factor is very sensitive to an offset in the x-direction. It even dips below 1, meaning the decay rate of the emitter will be lower than in a bulk sample. An offset in the z-direction does not seem to have a big impact on the Purcell enhancement.

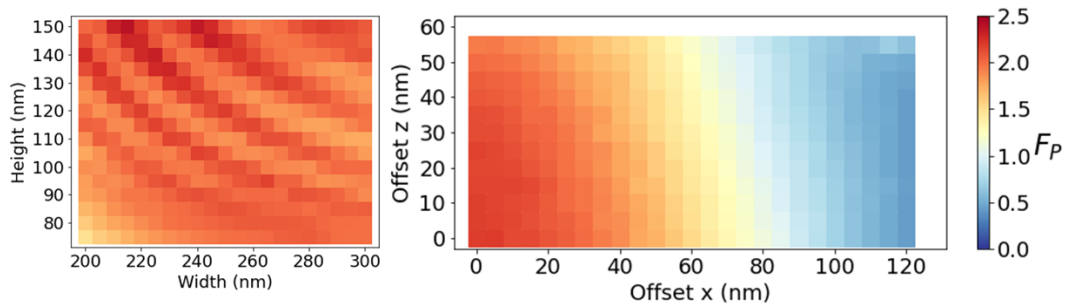


Figure 3.8: Purcell factors for  $\langle 110 \rangle$  waveguides. On the left, the results with a centered dipole for different waveguide sizes are shown. On the right, the results for a 250 nm x 120 nm waveguide with varying dipole offsets from the centre are shown. Color scales are the same for both figures.

The Purcell enhancement can in some cases be used to boost the Debye-Waller factor. This is possible because the Purcell factor could be different for emission of light with different frequencies. We can also test what the impact of this will be on these waveguides. In figure 3.9, the Purcell factor is calculated for light with a free-space wavelength of 620 nm (close to the ZPL) and longer wavelengths which appear in the PSB. The figure makes clear that the Purcell factor for these wavelengths is not significantly different in the waveguides. The Debye-Waller factor is therefore expected not to change from the bulk case.

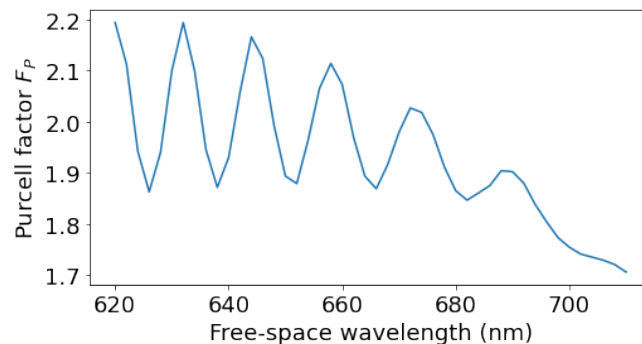


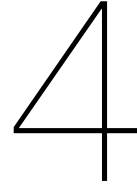
Figure 3.9: Purcell factor for photons emitted by a SnV centre in a 250 nm x 120 nm  $\langle 110 \rangle$  waveguide. The Purcell factor stays somewhere around 2 and starts to drop off more strongly around 700 nm. Since most of the PSB is emitted between 620-680 nm [20], this is no significant difference.

### 3.8. Conclusions for Optimal Waveguide Design

From the simulations, we can draw several conclusions for the waveguide fabrication process:

- **In terms of coupling factor  $\beta$ , waveguides along the  $\langle 110 \rangle$  crystal plane clearly outperform the waveguides along the  $\langle 100 \rangle$  plane.** In every simulation, the  $\langle 110 \rangle$  waveguides come out on top in terms of coupling between dipole and waveguide. This is also what is to be expected intuitively, as the dipole has no component in the direction along the waveguide anymore. During fabrication we noticed that the  $\langle 110 \rangle$  waveguides were not significantly more difficult to fabricate.
- **An ideal waveguide is relatively thin and wide, with a size of approximately 250 nm x 120 nm.** The highest coupling factors for waveguides in the  $\langle 110 \rangle$  direction is not all that sensitive to small changes in waveguide size, as long as it is in that region. It is important that the waveguides are larger in width than in height.
- **Good coupling factors can be reached even if the dipole is not located exactly in the centre of the waveguide.** The coupling factor is quite forgiving as to where the dipole is located exactly. For the  $\langle 110 \rangle$  direction, especially the vertical shifts do not change too much, but also the decrease from a horizontal shift is manageable. This is good, since we don't have very much control over the horizontal location. If we had no control at all over the location of the SnV and we assume they are uniformly distributed, there is still a 60% chance of  $\beta > 0.5$  and an 80% chance of  $\beta > 0.4$ .
- **The upper bound for waveguide size imposed by the single-mode regime is not limiting.** To ensure that a waveguide only allows a single mode to propagate, there is a maximum size we can make them. However, the optimal coupling factors are reached for even smaller waveguides, so this is not limiting. We can see that the transition to the multi-mode regime happens around 340 nm x 340 nm, while optimal coupling is reached for waveguides of sizes in the range of 200 nm x 200 nm to 250 nm x 120 nm. Large angles on the bottom of the waveguide restrict this a bit further, but do not get close to being a limiting factor. Even in a very extreme scenario with a bottom angle of  $45^\circ$ , the maximum size lies around 310 nm x 310 nm.
- **The Purcell factor of the emitter is roughly 2, but will not be used as a design criterium.** The Purcell factor is not an important figure of merit for the waveguide, but it is useful to have an estimation of how large it is. For waveguides that have been fabricated according to the criteria mentioned above, the maximum Purcell factor is in the range of 1.75 to 2.5.





# Experimental Determination of Parameters

For predicting whether a dip caused by the SnV centres will be visible in the transmission of the waveguides, we need to know certain parameters of the SnV centres that will be located in the waveguides. In order to make some estimations, I have measured some properties of the SnV centres located in the bulk sample in which we will later fabricate the waveguides. The parameters needed for a realistic simulation are the following:

- **Coupling  $\beta$ .** This is the coupling of the emitter to the waveguide that we will be able to reach. This was simulated in the previous chapter, and will have to be multiplied by 50% to account for the quantum efficiency and Debye-Waller factor of the SnV centre.
- **Optical Transition Decay Rate  $\Gamma$ .** This determines the minimum width of the transmission dip and also has its effects on the depth of the dip and critical photon number. Furthermore,  $n_\tau$  is defined as the mean photon number in the input field within the SnV lifetime, which depends on  $\Gamma$ .  $\Gamma$  could also change after waveguide fabrication because of an additional Purcell factor, which we estimated to be between 1.75 and 2.5.
- **Spectral Stability and Spectral Diffusion.** Ionisation of the defect will remove the line entirely. Determining the how long this takes depending on the input power allows us to make a prediction about which powers we can use in the transmission dip measurements, and how long the measurements can take. I will also model the spectral diffusion based on measurements.
- **Pure Optical Dephasing Rate  $\Gamma_d$ .** This parameter affects the width and depth of the transition dip, and also has impact on the critical photon number of the SnV centre. This parameter could be different in the waveguides compared to the bulk sample because of extra surface charges, but we know from literature that SnV centres in waveguides can have narrow lines [18]. We will also determine how this depends on input power and on temperature.
- **Saturation Power  $P_{sat}$ .** The spectral stability will vary depending on the input power. We can determine exactly how much power is reaching the defect, by finding its relation to the saturation power. The simulations of the transmission dip will determine at which fraction of the saturation power the S/N ratio will be the largest. From there I will determine the stability of the emitter at this power.
- **Taper Coupling  $\eta_T$ .** High laser power will saturate the emitter and decrease the transmission dip contrast. At low laser power, an inefficient taper coupling decreases the signal strength, leading to a lower signal-to-noise ratio. Knowing the taper coupling efficiency will allow us to determine whether our S/N-ratio will be high enough to see the transmission dip.
- **APD Dark Count Rate  $\gamma_{dark}$ .** Laser reflections and scattering will not play a large role in transmission measurements, so we suspect that most of the noise in the system will arise from dark counts on the APD.

All measurements on the SnV centres in bulk were carried out in a confocal setup which allows for resonant and off-resonant excitation, and allows for collection of the ZPL and PSB of SnV centres. The sample is a <100> grown electronic grade diamond. SnVs were implanted with 350keV, translating to 80nm depth. The dose was  $1e11$  ions/cm<sup>2</sup>, the sample was annealed at 1200°C. The setup for waveguide measurements is explained in section 4.5.

## 4.1. Optical Transition Decay Rate

In order to separate the contributions to the linewidth from the dephasing and from the lifetime limit, we need to measure the lifetime. We do this by shining the resonant laser on an SnV centre for a very short time interval, and subsequently record the photons emitted in the phonon side band (PSB). After repeating this many times, we divide the photon counts in several time bins and expect to see an exponentially decaying occurrence of photon counts.

I carried out this experiment for 9 different SnV centres in various locations in the sample and the lifetimes resulting from the exponential fitting are shown in figure 4.1 (blue data), along with the corresponding lifetime limited linewidths (secondary y-axis). The fits are quite good, resulting in small error bars. I suspect this is an underestimation of the real error since the pulse signal has not quite vanished in the measurements. (See appendix for individual measurements.) Also, the result seems to change when changing the time window for the fit. From the measurements, the lifetime limited linewidth is estimated at roughly  $\Gamma \approx 25$  MHz, which would be improved to roughly 50 MHz with the Purcell factors simulated before. The measurements for the broadened linewidth are shown in red. A typical measurement for this is shown in figure 4.2.

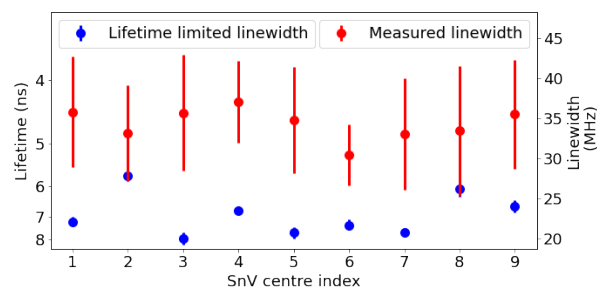


Figure 4.1: Excited state lifetimes and corresponding lifetime limited linewidths of 9 different emitters in the sample. Decay measurements were carried out as described in B.1, with 113 nW of red power and 10uW of green power. Red power for measuring the broadened linewidths of SnV's 1 through 5 was 1nW, and 0.5nW for SnV's 6 through 9, because the latter SnV's had brighter lines. The lifetimes are not that far off from the literature values of 5 - 7 ns [12, 22]. I suspect the deviation from this value can be attributed to having low signal strength and the pulse not entirely being suppressed.

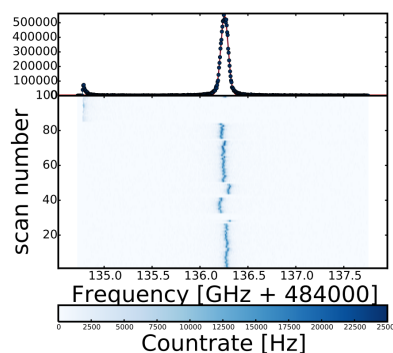


Figure 4.2: Linewidth measurement of a SnV centre. Scan taken at 0.8nW red power, only repumped with green laser when line disappeared. The average duration of the line here is 14.8 scans (29.6 seconds). The top part of the figure shows the summed up counts, the bottom part contains all the individual scans, where more counts are indicated by a darker shade of blue. It can be seen in the figure that the line sometimes disappears, and then later comes back because of a green repump.

## 4.2. Spectral Stability

SnV centres do not have a permanent electric dipole moment, making them first-order insensitive to electric fields. The higher-order response does still play a role, but only at large E-fields. There are two effects that I will take into account separately. First is the concept of 'blinking', or the disappearance of the line, possibly caused by (de-)ionisation of the defect [8]. Second is the spectral diffusion, or the movement of the peak of the transition line. In the following part, I describe how I have analysed the measurement data to determine an accurate way of implementing these effects in the simulations.

### Blinking

I have looked at the average number of scans that can be performed before the line disappears and the emitter has to be repumped. The results for different powers have been shown in figure 4.3. The jumps in the figure are due to new SnV centres appearing at higher powers. An example of what happens at SnV 1 is shown in figure 4.4. I excluded these data points from the fit.

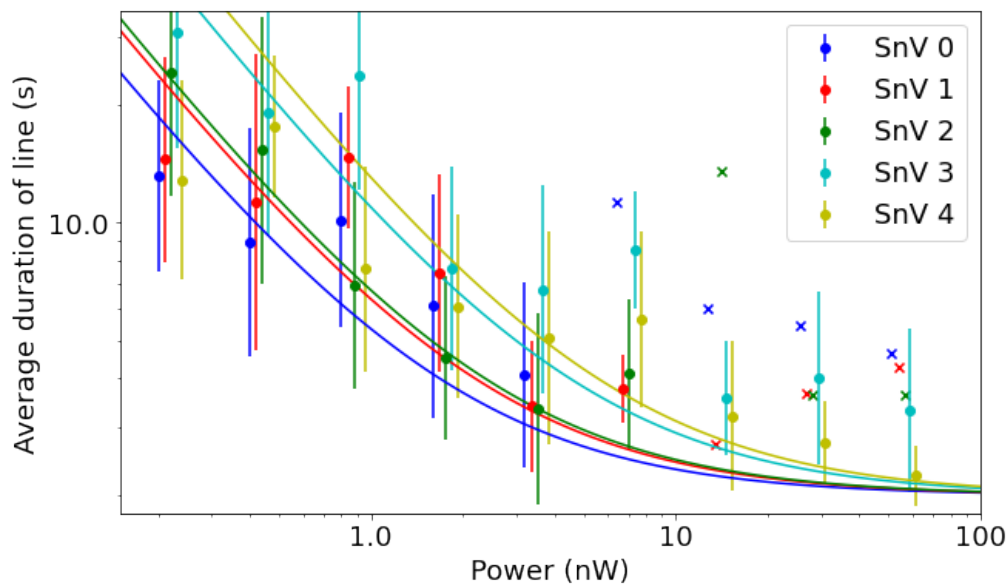


Figure 4.3: Stability for 5 different SnV centres for different powers. Lines are fitted to a curve  $y=c/x+2$  [s]. The offset is 2 seconds since the worst case stability is a disappearance after one scan. The fits are not very good, but we can conclude that at 0.2nW of laser power, most SnV centres remain stable on the order of 10 seconds. Crossed markers indicate the points where a new SnV centre appears in the scans, which are excluded from the fit. An example of when this happens at SnV 1 is shown in figure 4.4.

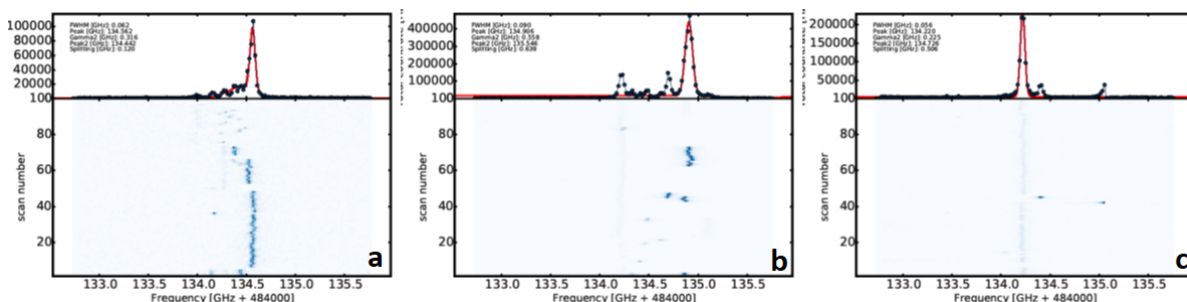


Figure 4.4: Example of a new SnV centre appearing at higher powers and starting to affect the results. (a) shows a measurement of a SnV centre. (b) shows the measurement for a higher power where the SnV is less stable. (c) shows a measurement at even higher power, where a new SnV centre has appeared, from which the script wrongfully concludes that the same SnV centre is now very stable.

## Spectral Diffusion

For the spectral diffusion we must have a measure for how much the line moves around before disappearing. Figure 4.5a shows the movement traces of recorded lines at different powers. Just like we saw when looking at the blinking, the traces for higher red power are generally shorter. Figure 4.5b shows overlapped histograms of the line locations for each power, fitted to a Gaussian. Surprisingly, the distributions don't differ that much, and there is no pattern that can be recognised. This is probably caused by the fact that, although higher power causes faster diffusion, the line has a shorter time to diffuse since it disappears more quickly.

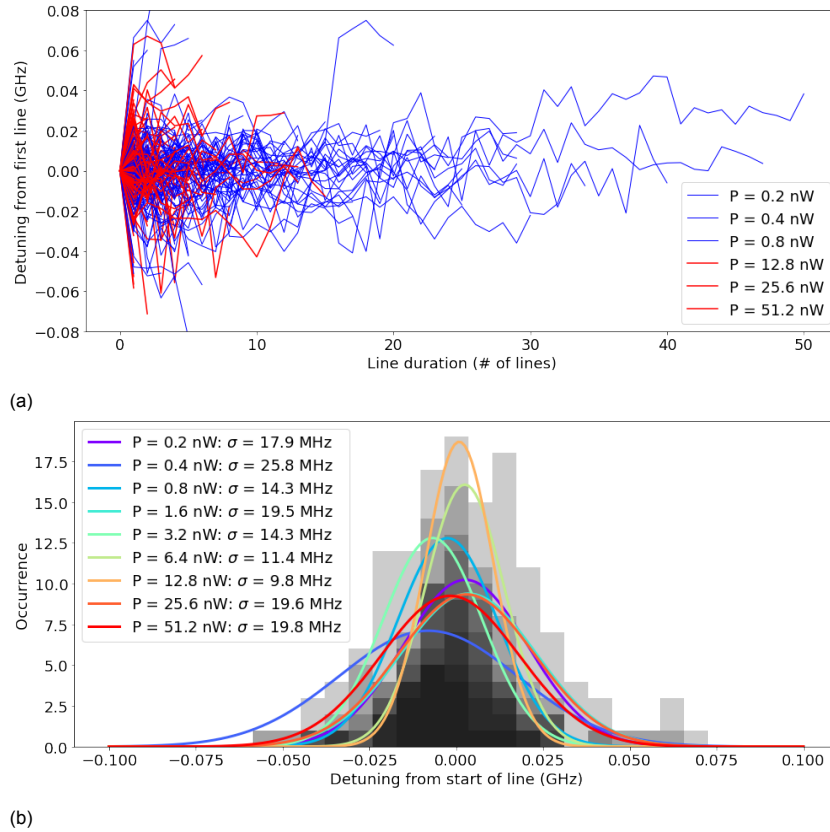


Figure 4.5: Examples of spectral diffusion of 5 different SnV centres, for various powers, 100 scans each. (a) shows traces of each separate line, relative to the start of the line. (b) shows a histogram of all the detunings for the different powers. Histograms are transparent and overlapped (not summed), fits are Gaussian.

For implementing this in the simulation, I can now separate these two effects. I will come back to the blinking in figure 4.3 to judge whether the line stays long enough to do the dip measurement for the required power. I will model the spectral diffusion as an effect independent of power, with a spread of 17 MHz, the average over the fits in the figure.

## 4.3. Pure Optical Dephasing Rate

We can measure the dephasing of the optical transition by comparing the linewidth of the transition to the lifetime-limited linewidth. I determined the linewidth of several SnV centres in the sample by performing 100 consecutive PLE scans over the optical transition for several different laser powers. These linewidths can be estimated for all SnV centres for different powers. The results have been shown in figure 4.6a.

Figure 4.6a also calculates at which red laser power the emitters saturate. The values are shown in the legend. This allows us to link the spectral stability of the SnV that we determined before, to the power that will interact with the defect as required by the simulations of the transmission dip. Some uncertainty remains in the saturation powers, since the error bars in the figure are large. It does however give an indication of the order of magnitude, and tells us that the linewidth is good in the regime that

is important for the transmission dip measurements (below saturation). I also tried a different way of measuring the saturation power, which is shown in figure B.3.

Figure 4.6b shows the temperature dependence of the linewidth. An increase in temperature results in a larger presence of phonons which can excite the SnV centre to the upper orbital branch of the ground state. We expect this process to be the main contribution to dephasing at low temperatures. The dephasing rate should be proportional to the excitation rate for this single-phonon process, which is [13]:

$$\gamma_+ = 2\pi\chi\rho\Delta^3 n_{BE}(\Delta, T) \quad (4.1)$$

Here,  $\Delta$  is the SnV ground state splitting of 850GHz, and  $\chi$  and  $\rho$  are proportionality constants for the interaction frequency  $|\chi_k(\Delta)|^2 \approx \chi\Delta$  and for the density of modes  $\rho(\Delta) \approx \rho\Delta^2$ .  $n_{BE} = 1/(\exp(\hbar\Delta/k_B T) - 1)$  is the Bose-Einstein occupation of phonons with energy  $\hbar\Delta$  at temperature  $T$ .

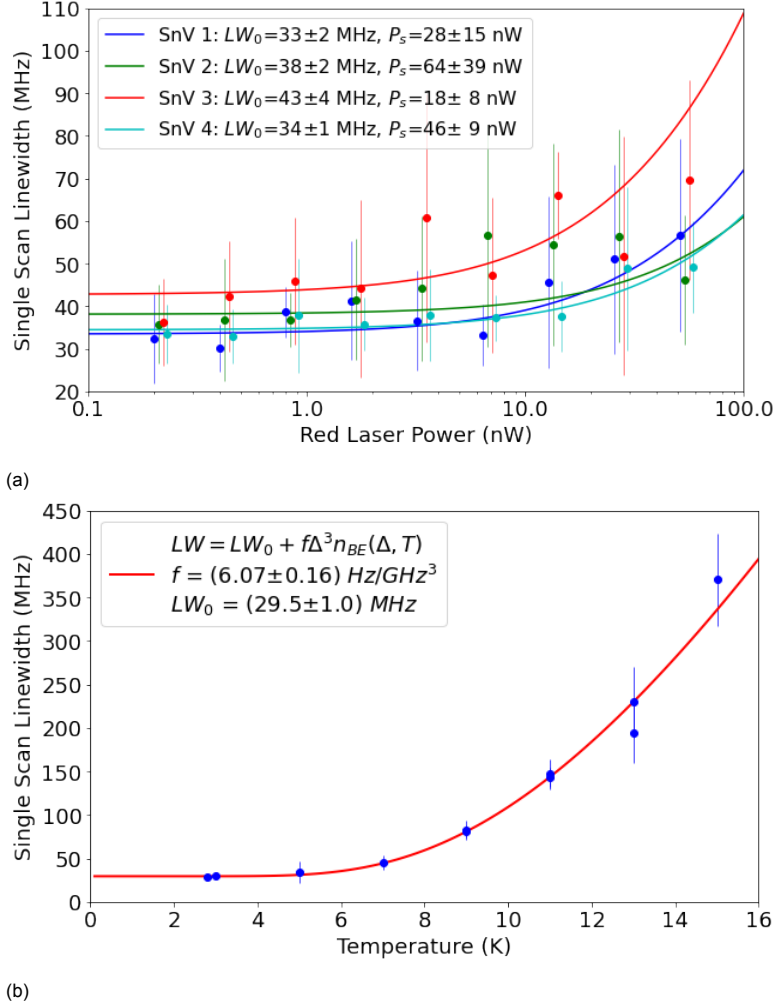


Figure 4.6: Linewidths including errors for different powers (a) and for different temperatures (b). 4 different SnV centres are shown in figure (a). Data have been offset slightly in the x-direction to make the error bars visible. It is clear that increasing the power also increases the linewidth. This is done for the same 5 SnV centres shown in figure 4.3. I manually excluded the measurements for a fifth SnV centre since it has a weird lineshape which does not fit a Lorentzian peak. The data for this centre can be found in appendix B.2. The lines indicate a fit to  $LW = LW_0\sqrt{1 + P/P_s}$ . (b) shows the temperature dependence of the linewidth, where the fit assumes a single-phonon process exciting to the upper orbital branch of the ground state.

A realistic value for the single-scan linewidth at low power in this sample is  $\Gamma + 2\Gamma_d \approx 35 \pm 5$  MHz. As for the temperature dependence, we have seen that we can obtain a temperature of 5K with the fibers mounted. From the fit, this leads to an estimated additional increase of  $3.2 \pm 2.0$  MHz. Taking the pessimistic ends of the confidence intervals from the results in the past two sections yields an estimate for the total dephasing of  $\Gamma_d \approx 10$  MHz.

## 4.4. Taper Coupling

For transmission measurements, we will need to optimise two taper couplings. The transmission that results gives an indication of the combined efficiency of the two tapers, but we get no information about the individual efficiencies. We will therefore start by optimising a single taper coupling.

### Single-Sided Taper Optimisation

We use waveguides which have a tapered end on one side, and a Bragg mirror on the other side. The reflected light is then the result of the square of the taper coupling efficiency, a constant factor of the reflectivity of the Bragg mirror, and other constant losses in the fiber system. The resulting structure is visualised in figure 4.7.

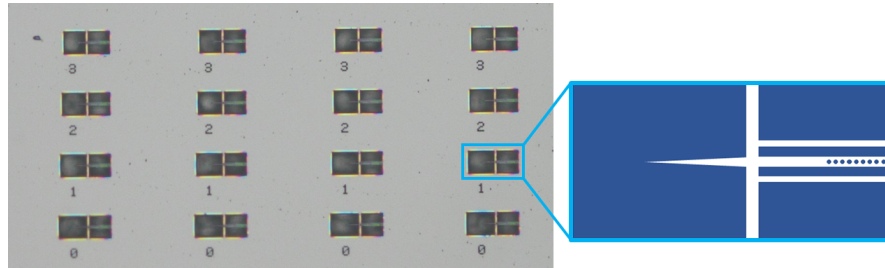


Figure 4.7: Structure for measuring the 1-sided taper coupling. On the left is an optical microscope image of an array of waveguides. The inset shows a schematic of what each waveguide looks like. Blue areas are a cut-out of the diamond. What remains is a waveguide with a tapered end on the left and a Bragg mirror on the right. It is supported by cross-beams on both sides. The extra beams parallel to the waveguide are redundancies from other plans that we had with the sample. The numbers on the microscope image indicate an index for the length of the taper. We will use this to find the optimal taper length for our system.

A schematic of the measurement setup for single-sided taper coupling is shown in figure 4.8. It shows the components that are relevant for the measurements. It also shows the definitions of  $P_{in}$  and  $P_{out}$ , along with the equation that relates them. The fraction of power that is transmitted for a certain wavelength is determined by the transmission of the beam splitter, the loss in the splice, the taper coupling efficiency, the reflectivity of the Bragg mirror for the wavelength, and the reflectivity of the beam splitter. The white laser, which sends out light with a broad spectrum, can be switched out for a red laser. For the measurements shown in the main text, the red laser has been used. In these measurements, the losses in the beam splitter have been corrected for, but not the losses in the splice or losses in fiber-fiber connectors. This will be done for the 2-sided coupling measurements.

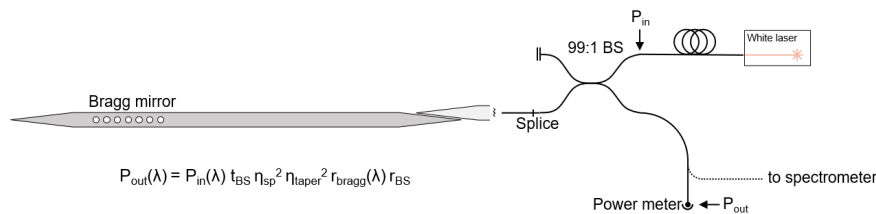
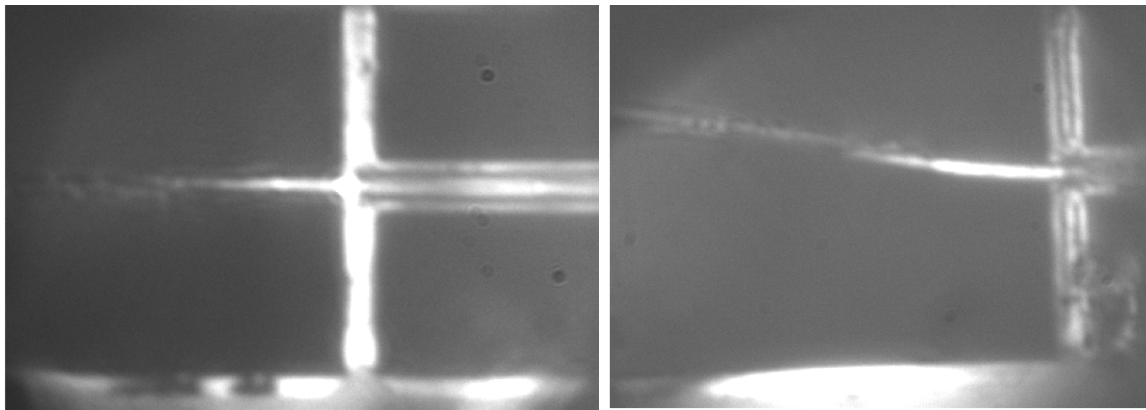


Figure 4.8: Schematic of the setup for reflection measurements.

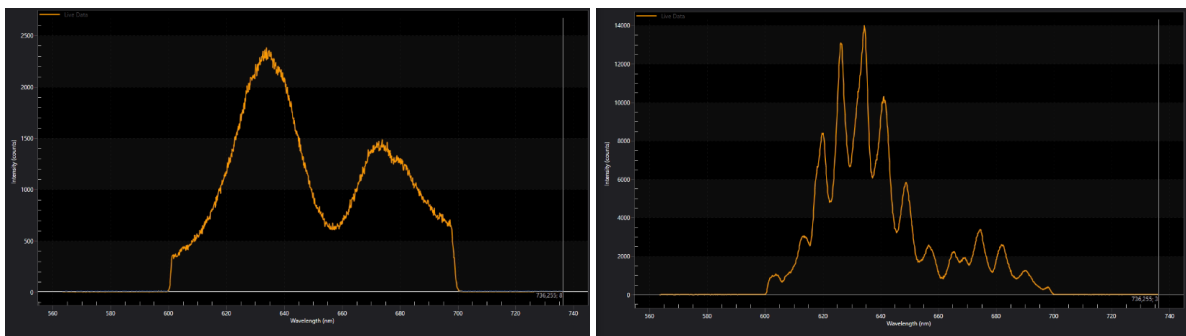
I found that the way to most consistently obtain a stable coupling was by making use of the Van der Waals force between the tapered fiber and the waveguide. This coupling is quite strong as can be seen in figure 4.9. The lengths of the tapers were determined using SEM images of the sample. From index 0 through 3 these were 11.29, 9.71, 8.00, and 6.50  $\mu\text{m}$  respectively. I had problems obtaining consistent coupling on the latter two sizes. Obtaining a strong enough attraction requires some overlap of the fiber with the waveguide.

In order to achieve minimal losses through the Bragg mirror, I compared the spectrum of a white laser (after a 600-700nm band pass filter) after reflection off the Bragg mirror to the spectrum of the input light. Both spectra are shown in figure 4.10. The spectra show that losses in the Bragg mirror reflection are minimized for light with a wavelength of 620nm (among some other suitable wavelengths, but 620 is obviously the most representative of the light we are interested in).



(a) (b)

Figure 4.9: Illustration of the Van der Waals force between the tapered fiber and the waveguide. The fiber was moved to the waveguide and subsequently pulled back in the direction that it came from.



(a) (b)

Figure 4.10: Comparison between the laser spectrum at the input (a) and the reflected light (b). The reflectivity of the Bragg mirror is based on a photonic band-gap. As a consequence, not all wavelengths are reflected effectively. Also, we suspect that the Bragg mirror together with the support structure creates a weak cavity which might affect this behaviour.

The resulting coupling factors achieved for the two suitable taper lengths, for various taper overlap lengths, are shown in figure 4.11. The resulting efficiency is not high. Other losses could have occurred in the splice and in fiber to fiber connectors. These have remained constant during the experiments for the results in the figure, and therefore do not affect the conclusions for optimal taper length and overlap. These results have been used in the next round of sample fabrication.

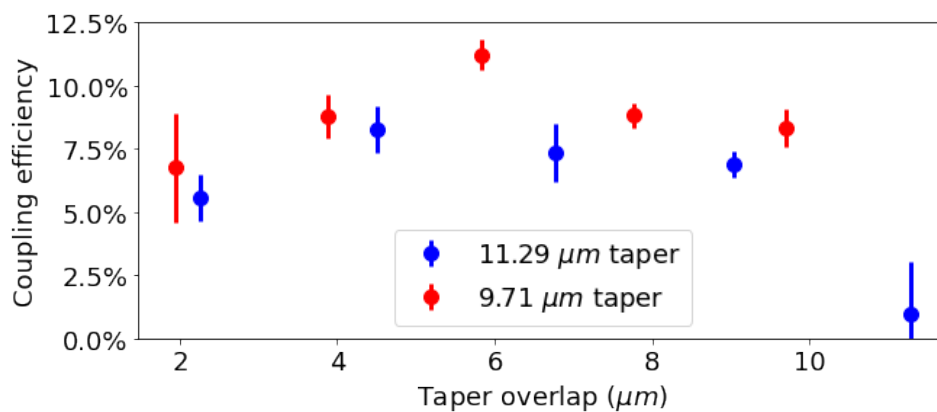


Figure 4.11: Resulting single-sided taper coupling factors. Laser light reflected by other imperfections was measured by disconnecting the tapers and measuring the reflection of the laser. This was subtracted from the results. The taper with length 9.71 μm shows the highest coupling efficiency of  $(11.2 \pm 0.6)\%$  around 6 μm overlap.

### Two-Sided Taper Coupling

The next step is checking whether we can also achieve taper coupling on two sides of the waveguides. For this we use a sample that contains many arrays of 10 waveguides each. This is illustrated in figure 4.12.

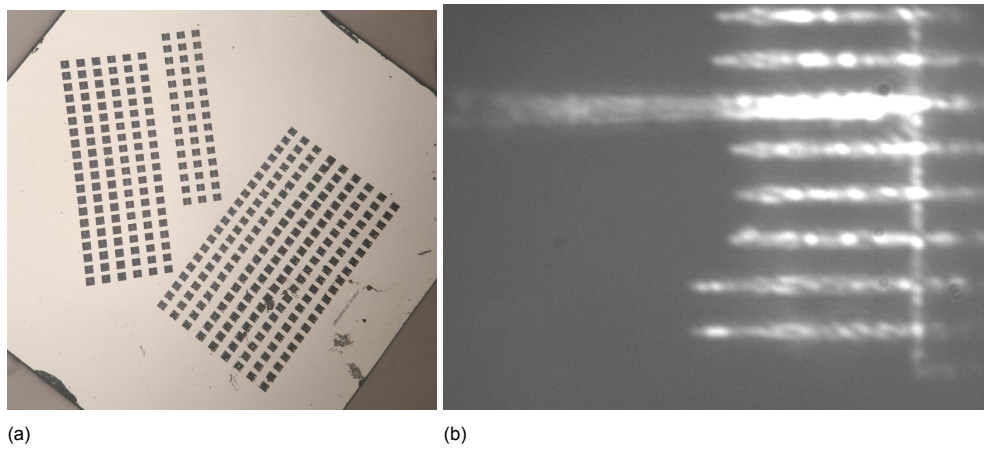


Figure 4.12: Structures for measuring the 2-sided taper coupling. (a) shows an optical microscope image of the arrays on the sample. Each small square is a cut-out that contains an array of 10 waveguides. The sample contains waveguides in both the  $\langle 100 \rangle$  and the  $\langle 110 \rangle$  directions. (b) shows a fiber which is taper-coupled to one side of a waveguide.

The windows in the cryostat cause optical aberrations when working with a high NA objective. However, the resolution of the imaging is too low when using an objective with low NA, as can be seen in 4.13a. This can be partly compensated by using an LED with shorter wavelength. The image using a blue LED and objective with  $NA=0.5$  is shown in figure 4.13b.

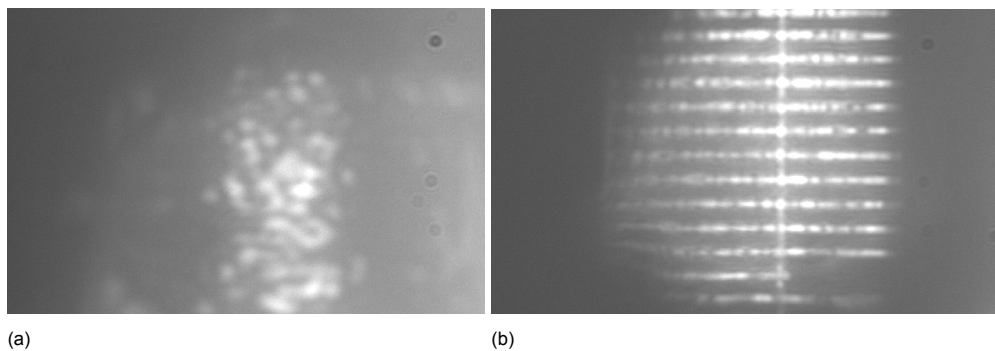


Figure 4.13: Waveguides used for 2-sided taper coupling. (a) shows an unclear image obtained with  $NA=0.5$ , (b) shows the image after changing to an objective with  $NA=0.8$ .

The setup used for these measurements is shown in figure 4.14. For these measurements, I also wanted to correct for the losses in the splices and in the fiber-fiber connectors. The setups used for this are shown in figure 4.15. We are interested in the efficiency of the taper coupling and would like to correct for the losses in splice 1, connector 1, and splice 2. For splice 1 and connector 1 this is straightforward. For splice 2, we cannot directly splice the beam splitter to a fiber, so we need to characterise the fiber-fiber connection 2 separately. Note that we can only use ratios between power, since the laser light fluctuates over the time that it takes to change the setup and splice the fibers. For the different subfigures, the ratios of power that we will measure can be described as follows, and it allows us to calculate a value for the efficiency of the taper coupling:

$$P_a/P_0 = \frac{r_{BS}}{t_{BS}} C_1 S_1 S_2 \eta_T^2 \qquad P_b/P_0 = \frac{r_{BS}}{t_{BS}} C_1 S_1 \qquad (4.2)$$

$$P_c/P_0 = \frac{r_{BS}}{t_{BS}} C_2 S_2 \qquad P_d/P_0 = \frac{r_{BS}}{t_{BS}} C_2 \qquad (4.3)$$

$$\eta_T^2 = \frac{(P_a/P_0)(P_d/P_0)}{(P_b/P_0)(P_c/P_0)} \qquad (4.4)$$

Where  $\eta_T^2$  is the total loss in the two tapers which are not necessarily equal.  $C_1, S_1, C_2,$  and  $S_2$  are the transmission coefficients of connectors and splices 1 and 2.  $r_{BS}$  and  $t_{BS}$  are the reflection and transmission coefficient of the beam splitter respectively. The fiber-fiber connectors have a different efficiency every time they are connected, so we have to carefully choose the order of doing the measurements.

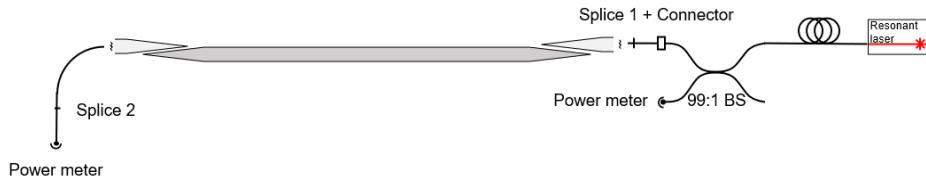


Figure 4.14: Setup for measuring 2-sided taper coupling efficiency. It shows the components of the setup, the locations where the power is measured, and all the locations where the largest part of the losses occur.

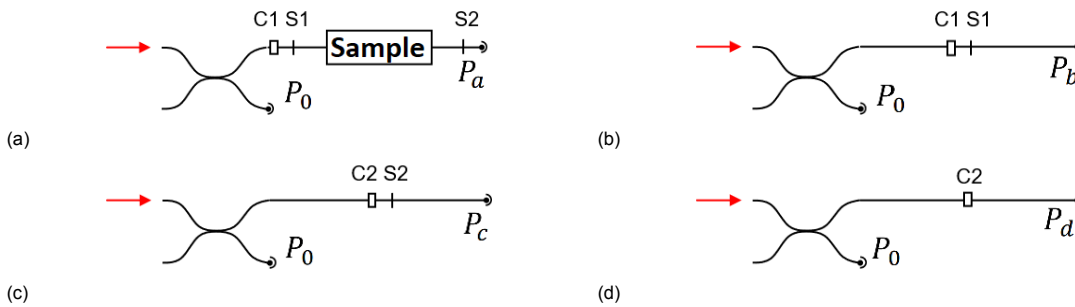


Figure 4.15: Setups used for measuring, in order to correct for losses in splices and fiber-fiber connections. (a) shows the measurement of  $P_a/P_0$  mentioned before in which the taper couplings contribute to the loss in the system. (b), (c), and (d) are measurements to correct for other losses in the system. Red arrow indicates the laser input.

The resulting coupling factors obtained for a different waveguides are shown in table 4.1.

Waveguide	Max 2 sided coupling	Average efficiency per taper coupling
1	0.0040(4)	(6.3±0.3)%
2	0.0075(7)	(8.7±0.4)%
3	0.0074(7)	(8.6±0.4)%
4	0.0030(9)	(5.4±1.5)%
5	0.0062(15)	(7.9±2.0)%

Table 4.1: Summary of 2-sided coupling factors for 5 different waveguides.

Though we can most likely see a transmission dip with these coupling factors (see next chapter), they do not get close to the near-unit coupling that we would eventually like to achieve or to the 50% coupling achieved in [3]. Below is a list of several factors which limit the achieved couplings, including recommendations to improve this further:

- The waveguides in this sample were likely multi-mode, which might lower the coupling efficiency. The waveguide widths are approximately 350 nm, but the thickness varies from 400 to 500 nm, with a large surface roughness. For the next samples, we try to make the waveguides small enough to only allow a single mode.
- The taper couplings were optimised manually. In the future we should have a script with a more sophisticated way of optimising both taper couplings in three dimensions.
- The waveguides are too close together. The Van der Waals binding of the fiber to the waveguides creates quite some hysteresis in the movement of the fiber. The distance needed to get the fiber loose is larger than the spacing of the waveguides. In future designs, we should have fewer waveguides per array.
- The fiber sometimes tends to touch the surrounding diamond before touching the waveguides with the tip. Etching a larger area in the direction of the waveguides should resolve this problem.

## 4.5. Experimental Setup

For measuring the transmission dip, we are working on a setup which has been shown in 4.16. For creating the taper coupling with the fibers, we want two piezo stacks inside the cryostat, one for each fiber. This is shown in figure 4.17. It also shows the heat shield which surrounds it, and the closed cryostat with fibers and electrical connections in the feedthroughs.

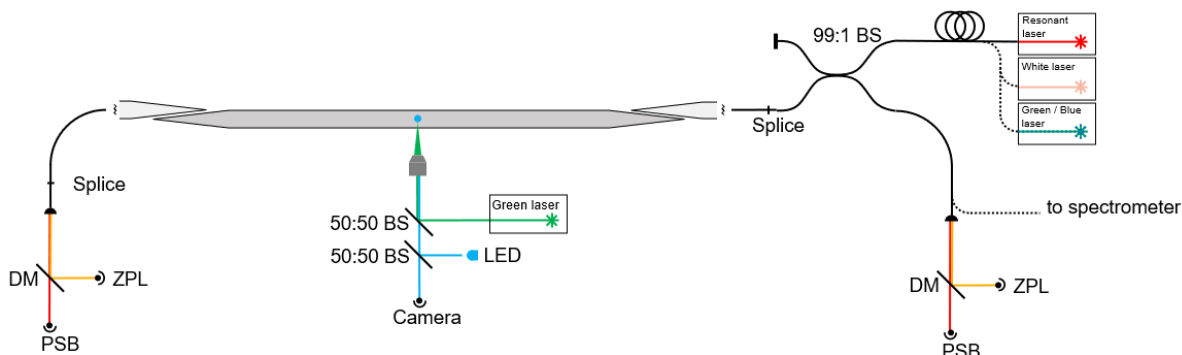


Figure 4.16: Experimental setup. Different lasers can enter the system via polarisation control and a 99:1 beam splitter. Both ZPL and PSB can be collected for the transmitted and reflected light. We use the free-space path for imaging and for off-resonant excitation.

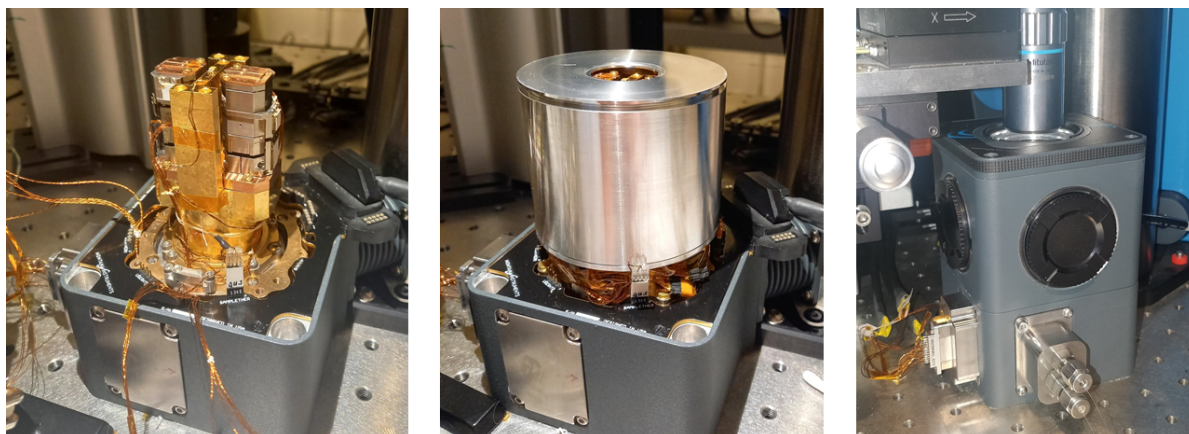


Figure 4.17: Inside of the cryostat where the fiber coupling takes place.

Left: fiber holders on top of piezo stacks, surrounding the sample platform. The sample platform is gold-coated to prevent oxidation which is detrimental for the thermal contact. Next to the sample, a temperature sample is mounted. The copper wires are the control for the piezos. Each piezo requires 2 connections for setting the position, and an additional 3 connections for reading out the position.

Middle: heat shield has been mounted over the fiber holders. It shields the insides from thermal radiation and is thermalised at 40K during operation. The top has a window to allow for free-space access via an objective. The window is coated to prevent most of the 273K thermal radiation from entering. Most of this radiation has significantly longer wavelength than the visible light that is of interest for the imaging. The electrical wires have been wrapped around the bottom of the sample holder stage.

Right: closed cryostat. The wires and fibers have been led through the appropriate feedthroughs. The objective above is the Multitoyo 0.5 NA objective. Seal is air-tight (pressure goes down to  $1.4 \times 10^{-5}$  mbar), and the temperature goes down to 5K.

## 4.6. APD Dark Count Rate

Whether we can eventually measure a visible transmission dip depends on the strength of the signal that we can get out of the system, compared to the noise. For some experiments, it is possible to run measurements with high input power, with many repetitions, or for a long time. This makes sure that the S/N ratio is higher, or that the noise cancels out on average. In this case, we are limited in time and in power that we can input by the spectral stability of the defect.

We suspect that most of the noise will arise from dark counts in the APDs. The measurement to obtain a realistic estimate for the dark counts was run by plugging a fiber into the APD with one end, as it will be done in the experiments too. The other end of the fiber was spliced to a tapered fiber which was mounted on the fiber holder in the cryostat. The lights in the room and the LED illuminating the sample were turned off, as we will do so too in experiments.

The count rate that was detected by the APD for 100 measurements of 1s each averaged out at:

$$\gamma_{dark} = 171.7 \pm 12.9Hz \quad (4.5)$$

The detections are assumed to be independent events that happen with a small probability in each time bin. The limit of this is the Poisson distribution. Figure 4.18 shows a comparison between the APD counts and a sample of the Poisson distribution that I will use in the simulation for the transmission dip.

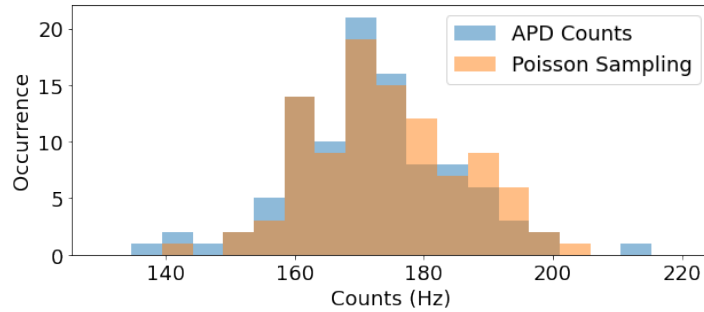


Figure 4.18: Comparison between the counts from the APD, measured in 100 measurements of 1s each, and samples from a Poisson distribution with expectation value of 171Hz. The close resemblance means that the Poisson distribution is a good approximation.

# 5

## Transmission Dip Simulations

### 5.1. Transmission Dip as a Function of Laser Power

The simulations for the transmission dip are set up to closely mimic an actual experiment. How this is implemented is described in appendix C. The parameters we used were estimated in the previous chapter and are summarized in table 5.1. The simulation is run for a range of laser input powers. A transmission on resonance of 1 means that no dip is visible, 0 means perfect reflection on resonance. The results are shown in figure 5.1.

Parameter	Sign	Value	Unit
Emitter-waveguide coupling	$\beta$	0.2	
Single taper coupling	$\eta_T$	0.1	
Lifetime limited linewidth	$\Gamma$	50	MHz
Dephasing	$\Gamma_d$	10	MHz
APD dark count rate	$\gamma_{dark}$	171.7	Hz

Table 5.1: Parameters used for the transmission dip simulation.

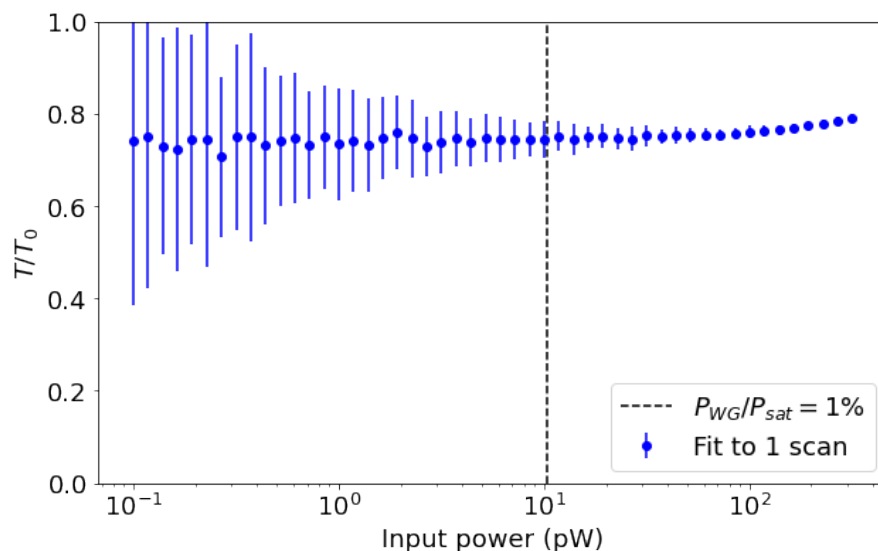


Figure 5.1: Transmission on resonance of the SnV-waveguide system, as a fraction of the off-resonant transmission. 1 means no dip, 0 means total reflection on resonance. Simulation is run for multiple input powers, and a fit is made to a Lorentzian line shape. The fit has a large error for low powers due to a low S/N ratio. For higher powers, we can see the emitter starts to saturate. NB: the error bars are not uncertainties in how large the induced non-linearity will be, but a confidence interval we can expect from a Lorentzian fit after an experiment. The optimal result is 75(4)%.

We see that there is an optimal power. Too little laser power will result in a low signal to noise ratio, too much results in saturation of the emitter which also makes the dip more shallow. For the chosen parameters, the optimum is found approximately at  $P/P_{sat} = 1\%$ . This is determined by checking the values for  $n_r/n_c$  for the data points. At this power a transmission of 75(4)% is predicted.

The most important question is whether we expect the SnV centres to remain spectrally stable within the time that this measurement takes. Judging by the figure, we are interested in the stability of the SnV centres when scanning over their resonance with laser light at 1% of their saturation power. Looking back at the results from figure 4.6a, this power lies somewhere in the range from 0.1-0.7 nW for the measured SnV centres. Considering the stability of the SnV centres displayed in figure 4.3, we can check for each SnV centre that the stability of their lines at these powers exceeds 10 seconds. This is more than enough to be able to carry out the experiment before the line disappears. We should therefore be able to see a transmission dip with transmission of 75(4)% on resonance, assuming all parameters mentioned above will remain accurate after fabrication of the waveguides.

## 5.2. Improvement of Waveguide-Emitter Coupling

For the coupling, I now assumed a relatively safe value of 0.2, which we should be able to obtain pretty consistently judging by the earlier simulations. If we do post-selection on the waveguides containing particularly strongly coupled SnV centres, we could improve this to  $\beta \approx 0.4$ . Further into the future, we may be able to find a way to boost the ZPL emission while suppressing the PSB. In that case, we might be able to optimise towards  $\beta \approx 0.79$ . With stronger couplings, we could obtain a larger non-linearity. The result for different coupling values is shown in figure 5.2.

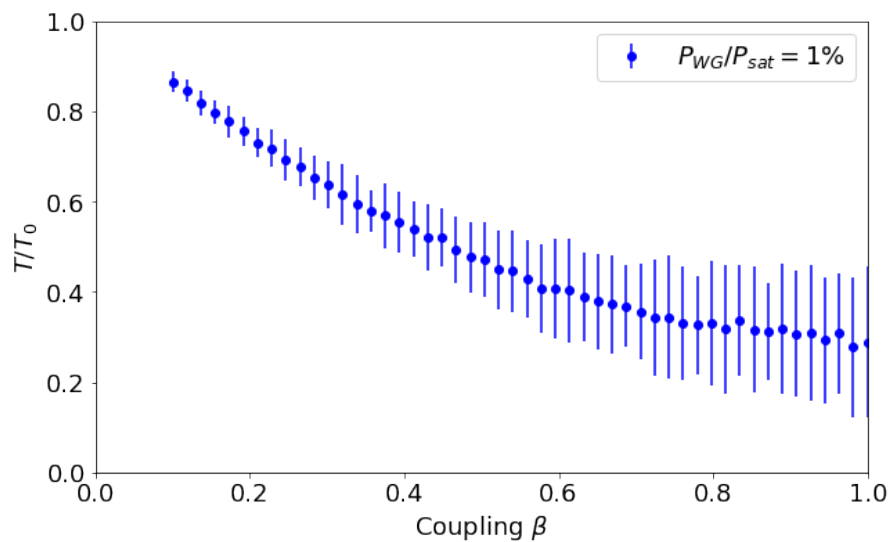


Figure 5.2: Dependence of transmission dip on coupling  $\beta$ . The transmission dip becomes deeper as the coupling gets stronger. We can reach 32(14)% for  $\beta \approx 0.79$

### 5.3. Improved Taper Coupling

The simulation in the main text is run for  $\eta_T = 0.1$ , or a very inefficient taper coupling. However, we can also run it for perfect taper coupling, but this does not improve the results much as is shown in figure 5.3. The S/N ratio is higher since less signal is lost, meaning we need less input power and we can work further below saturation. However, the transmission dip is not significantly deeper.

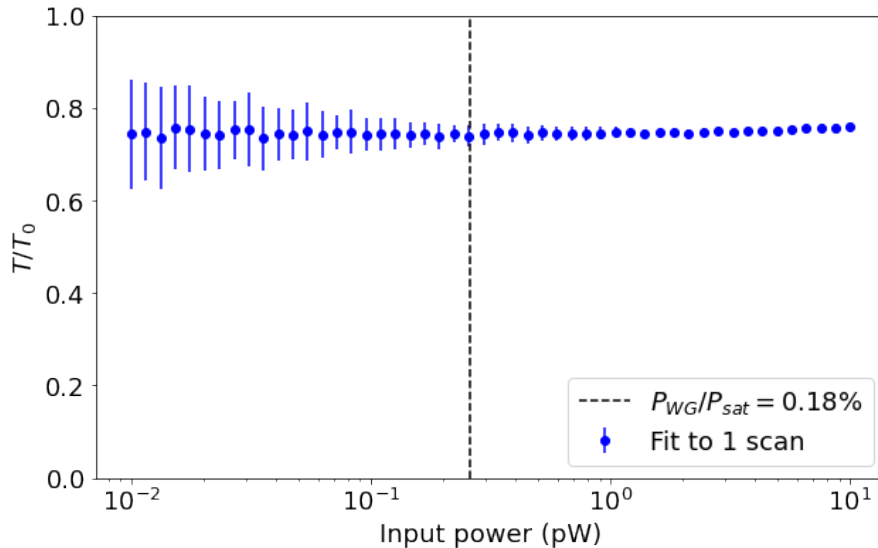


Figure 5.3: Transmission on resonance for different powers, with  $\eta_T = 1$ . The optimal value here is 74(2)%, which is not a big improvement over the 75(4)% at  $\eta_T = 0.1$ .

### 5.4. Repeated Measurements

Instead of choosing a power close to saturation, we can also choose a lower power and repeat the frequency sweep many times (or do a slower sweep). This has also been simulated, and the results for different numbers of repetitions is shown in figure 5.4.

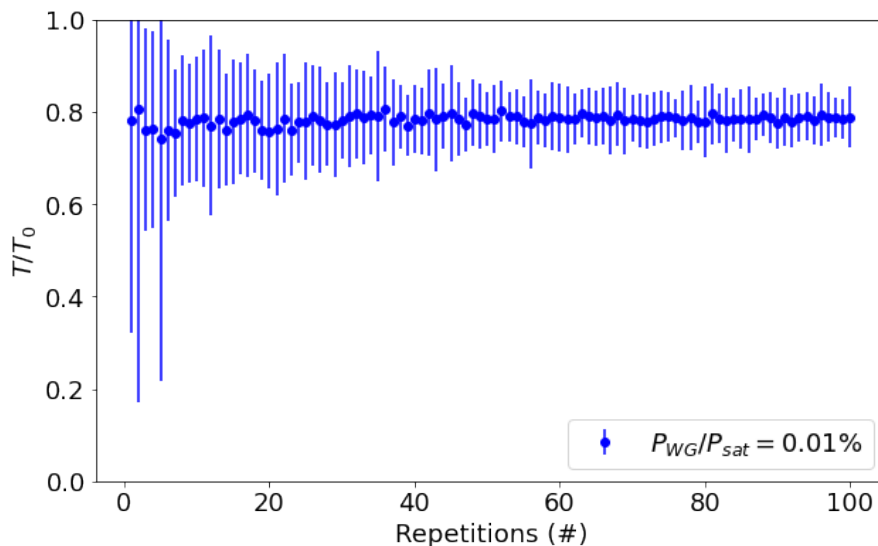


Figure 5.4: Transmission dip results for different numbers of repetitions of the experiment. We can see that the uncertainty in the fit becomes somewhat smaller, while not being at the cost of saturating the emitter. However, we cannot get the uncertainty down to the levels achieved at higher powers. This is due to the effect of the spectral diffusion at longer time scales. Also, there is a large chance the emitter will disappear during 100 scans, even at low power.



# 6

## Conclusion & Outlook

The results of the simulations from last chapter predict that we will indeed be able to measure a transmission dip with a contrast of  $\Delta T/T = 25\%$ . But for this to be the case, many assumptions must turn out to be valid. Will the dephasing rate of the emitters stay the same after waveguide fabrication? Will the Purcell factor indeed be approximately 2? Will we be able to obtain  $\beta \approx 0.2$ ? These are only examples of the unknowns. Previous work on group IV color centres makes us optimistic [3, 5, 18, 19].

Apart from this, the predicted contrast of the dip is definitely not optimal. From the simulations, we could see that there is one particularly effective improvement that can be made to enlarge the contrast: a larger  $\beta$ . This can be done by post-selecting waveguides containing SnV centres which have a strong coupling, and by boosting the ZPL emission of the SnV centres.

There are also improvements we can make which don't necessarily improve the transmission dip, but will become important on the longer term. The taper coupling efficiency, for example, doesn't impact the contrast of the dip (see Appendix C), but it will become an important photon loss contribution if we start using this for entangling the emitter with a single photon. An inefficient taper coupling will lead to a great reduction in entanglement generation rate in such a case.

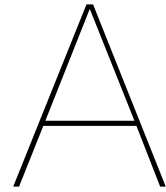
Strongly coupled SnV-waveguide systems will open up new possibilities for engineering a useful quantum internet [24]. As discussed in the introduction and theory chapters, SnV centres have many advantageous properties when it comes to building a quantum internet. However, SnV centres also come with their own challenges, which should be investigated further in the coming years:

- There are still many unknowns about the dynamics of the SnV centre and the interactions with its surroundings. As mentioned before, the model for the electronic structure is currently being revised. The decoherence and ionisation mechanisms are also not yet completely clear. Recently, Görlitz c.s. were able to provide some insight into one mechanism, including a way of overcoming it [8], but there remains a lot to be done.
- Coherent driving of the prospective qubit states has not been demonstrated very reliably. The inefficient transition between the two levels may be overcome by strain tuning. Once this is established for bulk samples, we should also look at how to engineer this in the waveguides. We could then look into spin-state-dependent reflection of single photons by an SnV centre. This step will be essential in making the SnV useful as a qubit.
- The first-order insensitivity to electric fields makes DC Stark tuning of the SnV centre more difficult. We will need to find a different method of adjusting the resonance frequency, or this might become a problem for generating heralded spin-spin entanglement between SnV centres.

These are some improvements that could enhance the transmission dip that we can see, or make these experiments more interesting. Next to these, there are some challenges that must be faced when turning SnV centres into useful building blocks for scalable quantum network nodes:

- The SnV centre optical transition energy corresponds to a photon in the visible spectrum. These 619nm photons have a large attenuation rate in optical fibers. Since compatibility with existing fiber-optic infrastructure would make setting up additional, distant connections way more efficient, it would be very advantageous to be able to efficiently convert these 619nm photons to telecom photons while retaining their phase.
- The spin dephasing time of SnV centres is too short for use as a memory qubit. A problem with current quantum network experiments is that entanglement is lost more quickly than it is generated. There are multiple ways to overcome this problem, but memory qubits offer a particularly attractive option. Carbon-13 spins are naturally present in diamond. Making use of this could improve coherence times of the stored entanglement, and provide the possibility of storing multiple entangled pairs of qubits per communication channel.
- Controlling single SnV centres per network node will result in an impractically low quantum information bandwidth. Multiple SnV centres in waveguides, control electronics, read-out devices, and photon routing paths could all be integrated on chips to increase this in the future.

It will take time and effort before these challenges are overcome. Other problems might arise, but up until this point we have not seen a show stopper. The progress seen so far is promising, and qualifies SnV centres as apt candidates for a future quantum internet.



# Waveguide Simulations Methods and Settings

## A.1. Finding the Single Mode Regime

The simulation uses the electromagnetic waves, frequency domain physics in the radio frequency package in COMSOL Multiphysics. A mode analysis is done in a 2D geometry representing a cross-section of the waveguide. This study finds all allowed modes for a given set of parameters.

The geometry consists of a polygonal waveguide cross-section surrounded by a rectangle of air. The waveguide material is polycrystalline CVD diamond by Dore et al. from 1998 [7]. This material contains optical properties measured in the infrared spectrum, but this results in relative errors of  $<1\%$  and therefore insignificant with respect to fabrication errors. The air surrounding the waveguide has a refractive index set to exactly 1. Some experiments will be carried out in vacuum and some other will be in air, but this does not significantly change the optical properties of the surrounding material ( $<0.03\%$  error).

A scattering boundary condition is applied to the outer boundaries. These boundaries only allow outward travelling waves and therefore do not create any reflection effects on the modes that can be found. The mesh is created based on the physics of the problem.

COMSOL usually finds two first-order modes. These correspond to the two different polarizations of the electric field. These have been shown in figure A.1 (a) and (b). If these modes are the only modes found, we consider this to be the single mode regime. If COMSOL is able to find more than two modes, we consider it to be the multimode regime. The modes are shown in figure A.1 (c) and (d).

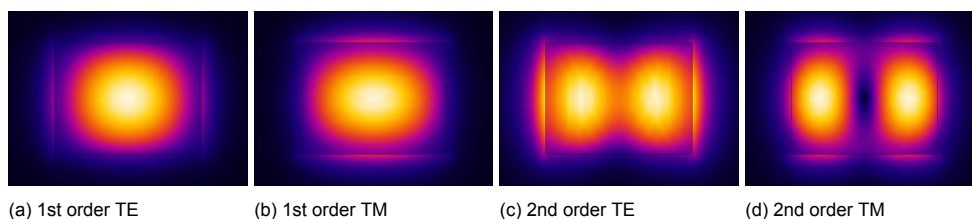


Figure A.1: Resulting modes from the COMSOL simulations. Lighter colors indicate a higher electric field norm. It can be seen from all figures that the mode is mostly contained inside the waveguide, but is also partly guided in the evanescent field just outside the waveguide. Waveguide size is  $460\text{nm} \times 350\text{nm}$ . For smaller waveguides, COMSOL only finds modes (a) and (b), indicating we are in the single-mode regime.

From these figures, one might notice that the 1st order modes are in general localized more within the waveguide than the 2nd order modes. This was confirmed in the COMSOL data, as the 2nd order modes structurally had lower values of their effective refractive index. This makes a useful way of distinguishing the single-mode from the multi-mode regime. Simply plotting the lowest refractive index of all modes COMSOL can find results in a steep drop when transitioning to the multi-mode regime.

The bottom angle on the waveguides have also been varied, as shown in the figures in the main text. The separate figures are shown in figure A.2.

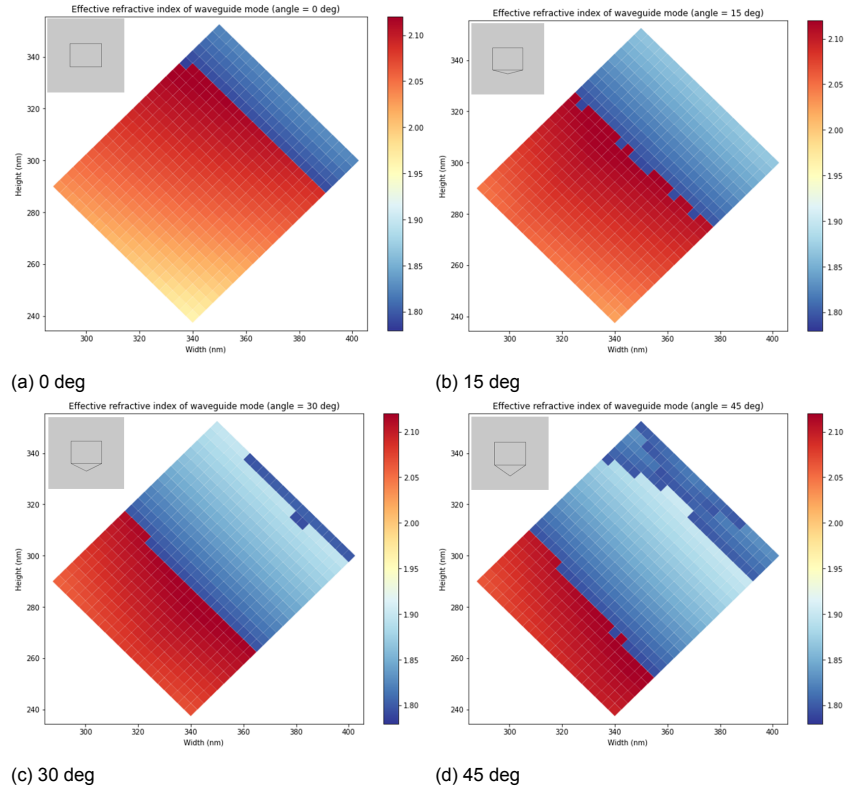


Figure A.2: Transition from single-mode to multi-mode regime for different bottom angling. The top left of each figure shows what a typical cross-section looks like.

## A.2. Finding the Coupling Factors for the Waveguides

For this simulation, we also use the EM waves, frequency domain study in the radio frequency physics package of COMSOL. The domain is now modeled in 3D. The same waveguide design as shown in figure 3.1 (b) is used, but now it is fully modeled in 3D. The defect is modeled as a dipole emitter. The material settings are the same as in the previous simulation. The same scattering boundary condition is applied to the outer boundaries and the mesh is again controlled by the physics of the problem. The electric dipole is entered as  $\mathbf{j} = -i\omega\mathbf{p}_0$ , since COMSOL requires a current dipole.

A quick test we can do, is to see what happens to a waveguide when only a tiny amount of light can escape. We do this by increasing the refractive index ratio. We expect the coupling to approach 1 if the ratio is increased to infinity, since most of the light should remain inside the waveguide. Figure A.3 shows the result for a refractive index ratio of 7.5. The resulting coupling into the waveguide 95% is an indication that this is indeed that case. From the picture it is also clear that these are two cosine waves in superposition, which signifies that both the TE and the TM mode are excited.

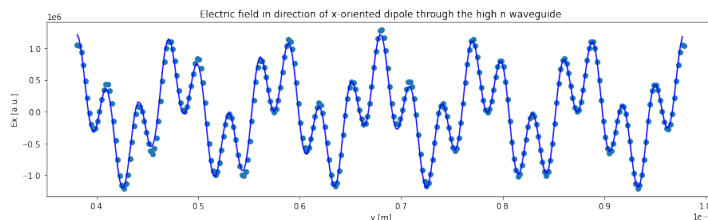


Figure A.3: Result of a waveguide where the index ratio is 7.5 instead of 2.4. The coupling achieved is 95%. This shows that the coupling does indeed approach 1 if all light stays confined in the waveguide.

## Waveguide coupling results

The optimal regimes for emitter to waveguide coupling were found by doing a large sweep of the width and height of the waveguides. This is shown in figure A.4. It also seems that square waveguides (on the diagonal) achieve the largest couplings. But there is a catch here. Because of the way in which the coupling is calculated (see section before), it becomes increasingly difficult to distinguish the couplings to the TE and TM modes as the wavelengths become more similar. In case the waveguides are roughly square, we can see from symmetry (and also from the data) that these wavelengths will become the same. This means the coupling factors for the square waveguides are overestimated.

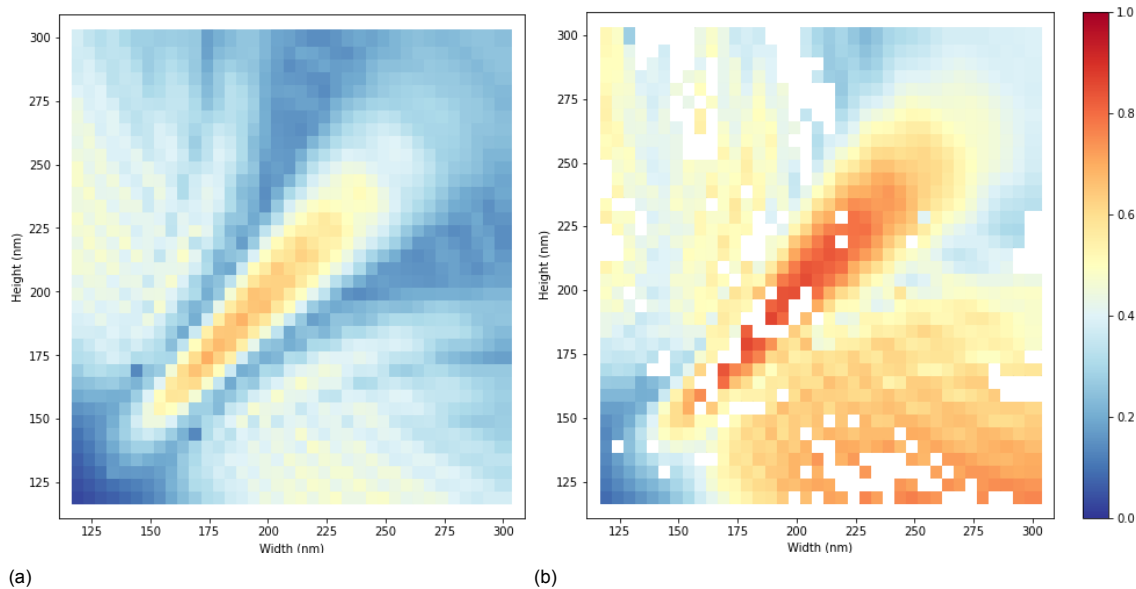


Figure A.4: Coupling factors  $\beta$  between dipole and waveguide. (a) and (b) show the  $\langle 100 \rangle$  and the  $\langle 110 \rangle$  waveguides respectively. A large area was swept to find where the coupling is largest.

## Coupling for Different Wavelengths

Some fringes are visible in the coupling simulations. These seem to be caused by some kind of interference effect, but it is unclear what exactly is causing this. In figure A.5 a comparison is shown with the same simulation where the free-space wavelengths has been set to 610 nm. This shifts the fringes with roughly 15 nm in this regime. The fringes in the coupling are not as pronounced as in the Purcell factor, but it is good to know that transitions with different energies might couple differently to the waveguide mode.

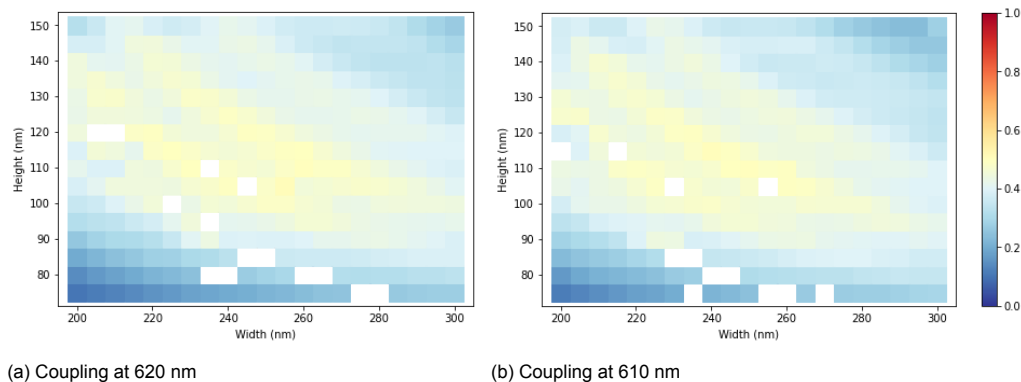


Figure A.5: Coupling to  $\langle 100 \rangle$  waveguides with varying sizes, simulated for light with 620 nm and 610 nm free-space wavelengths.



# B

## Supporting Information Experiments

### B.1. Optical Transition Decay Rate

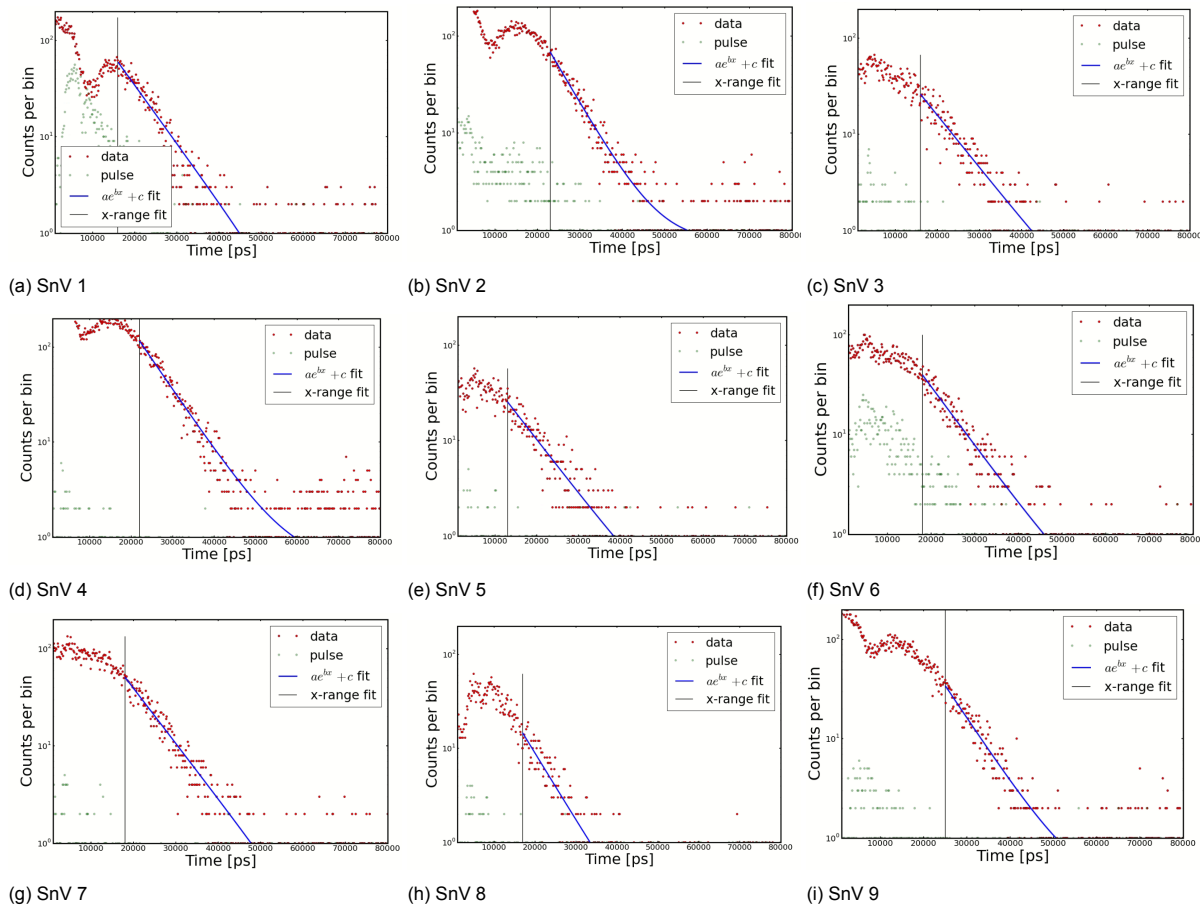


Figure B.1: Lifetime measurements of 9 different SnV centres throughout the sample.

For measuring the excited state lifetime of around 6 ns, we want to excite the emitter from the ground to the excited state, and subsequently measure the time it takes for an emitted photon to be detected. We should however make sure that the signal we measure does indeed originate from the emitter decay, and is not just scattered or reflected laser light. We therefore require a very short laser pulse. The AOM (acousto-optic modulator) which is usually used to control the laser power, cannot switch the power on and off fast enough. We therefore also use an EOM (electro-optic modulator) to create a very sharp pulse.

## B.2. Pure Optical Dephasing Rate

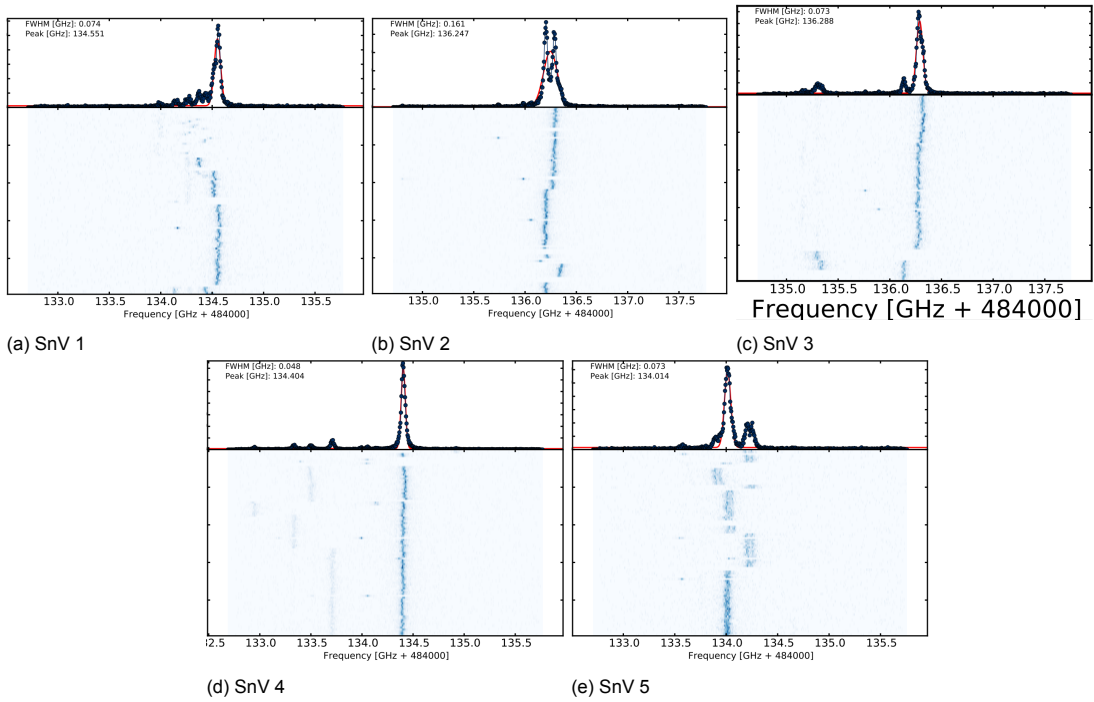


Figure B.2: Measurements of 100 lines each of the 5 different SnV centres, all at 0.2nW red power. Only 10uW of green power when line disappears. Figure (e) shows the data for SnV5, which has been omitted in the figure in the main text. It shows a weird double-peak line shape which does not fit well to a Lorentzian. It is therefore not possible to determine the linewidth from these data. I don't know what causes the double line shape.

## B.3. Saturation Power

A different way of measuring the saturation powers of the defects is by looking at how much fluorescence is picked up as a function of input power. At some point, the defects become saturated and the fluorescence doesn't increase when increasing the laser power. A plot of this is shown in figure B.3. The results are quite different from the results in the main text. A possible cause of this is fluctuation of the red laser power. This creates a mismatch between the values on the x-axis and on the y-axis.

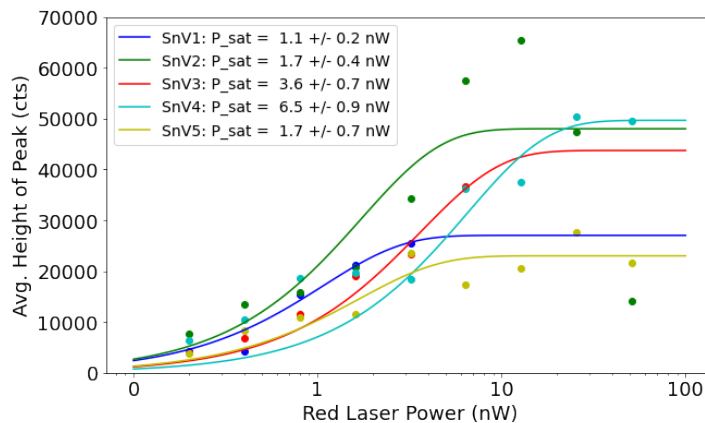
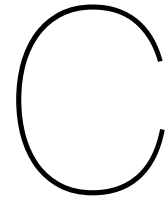


Figure B.3: Fluorescence counts for different red powers on 5 different SnV centres. Fit to  $y = y_{max}(1 - \exp(-P/P_{sat}))$ . Values from the fit are not accurate because of fluctuations in the red laser power.



# Transmission Dip Simulations

## Simulation Setup

In the experiments, a voltage controlling the frequency of the laser is swept, collecting counts from the APD in several time bins. The simulation will calculate the rate of photon emission into the system as a function of the input power. It also calculated the theoretical transmission probability based on the equations in the theory section, corrected for the losses in the taper couplings. It samples a Poisson distribution to determine the number of counts which end up in this time bin. It also samples a Poisson distribution of the dark counts and adds this to the signal. A single scan takes 2 seconds, just as in the linewidth measurements. The mean photon number in the waveguide mode is determined by multiplying the rate of photon emission with the losses in one of the tapers. Once the counts have been collected for each time (or equivalently, frequency) bin, the data is fit to a Lorentzian peak around 0 detuning.

For the spectral diffusion, I have sampled a new centre of the peak for each repetition of the experiment from a normal (Gaussian) distribution. If all the results from the repetitions are added up, this will lead to broadening of the peak, and it will be less deep. The shape is also not Lorentzian anymore, but (for many repetitions) a convolution of a Gaussian with a Lorentzian. This might be the reason for the uncertainty in the fit that remains for a high number of repetitions (see figure 5.4). For experiments with 1 repetition, there is no effect of the spectral diffusion. I find this justified since the single line scans to find the dephasing rate were carried out in exactly the same time, meaning that this effect is already present in the width of the original line.

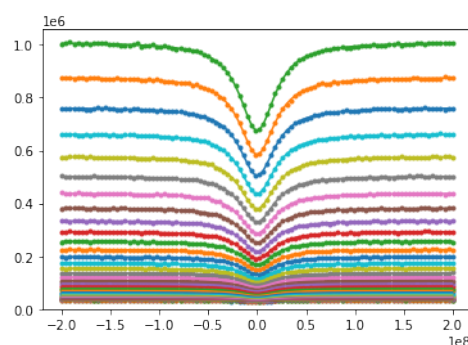


Figure C.1: Transmission dips for 33 different powers resulting in figure 5.1.



# Bibliography

- [1] Alexia Auffèves-Garnier et al. “Giant optical nonlinearity induced by a single two-level system interacting with a cavity in the Purcell regime”. In: *Physical Review A* 75.5 (May 2007), p. 053823. DOI: 10.1103/PhysRevA.75.053823. URL: <https://link.aps.org/doi/10.1103/PhysRevA.75.053823> (visited on 12/21/2021).
- [2] David D. Awschalom et al. “Quantum technologies with optically interfaced solid-state spins”. en. In: *Nature Photonics* 12.9 (Sept. 2018), pp. 516–527. ISSN: 1749-4893. DOI: 10.1038/s41566-018-0232-2. URL: <https://www.nature.com/articles/s41566-018-0232-2> (visited on 09/13/2021).
- [3] M. K. Bhaskar et al. “Quantum Nonlinear Optics with a Germanium-Vacancy Color Center in a Nanoscale Diamond Waveguide”. In: *Physical Review Letters* 118.22 (May 2017), p. 223603. DOI: 10.1103/PhysRevLett.118.223603. URL: <https://link.aps.org/doi/10.1103/PhysRevLett.118.223603> (visited on 09/13/2021).
- [4] Carlo Bradac et al. “Quantum nanophotonics with group IV defects in diamond”. en. In: *Nature Communications* 10.1 (Dec. 2019), p. 5625. ISSN: 2041-1723. DOI: 10.1038/s41467-019-13332-w. URL: <https://www.nature.com/articles/s41467-019-13332-w> (visited on 09/13/2021).
- [5] Michael J. Burek et al. “Fiber-Coupled Diamond Quantum Nanophotonic Interface”. In: *Physical Review Applied* 8.2 (Aug. 2017), p. 024026. DOI: 10.1103/PhysRevApplied.8.024026. URL: <https://link.aps.org/doi/10.1103/PhysRevApplied.8.024026> (visited on 09/16/2021).
- [6] David P. DiVincenzo. “The Physical Implementation of Quantum Computation”. In: *Fortschritte der Physik* 48.9-11 (2000), pp. 771–783. DOI: 10.1002/1521-3978(200009)48:9/11<771::AID-PROP771>3.0.CO;2-E. URL: <https://onlinelibrary.wiley.com/doi/abs/10.1002/1521-3978%28200009%2948%3A9/11%3C771%3A%3AAID-PROP771%3E3.0.CO%3B2-E>.
- [7] Paolo Dore et al. “Infrared properties of chemical-vapor deposition polycrystalline diamond windows”. EN. In: *Applied Optics* 37.24 (Aug. 1998), pp. 5731–5736. ISSN: 2155-3165. DOI: 10.1364/AO.37.005731. URL: <https://www.osapublishing.org/ao/abstract.cfm?uri=ao-37-24-5731> (visited on 11/17/2021).
- [8] Johannes Görlitz et al. “Coherence of a charge stabilised tin-vacancy spin in diamond”. en. In: *npj Quantum Information* 8.1 (Apr. 2022). Number: 1 Publisher: Nature Publishing Group, pp. 1–9. ISSN: 2056-6387. DOI: 10.1038/s41534-022-00552-0. URL: <https://www.nature.com/articles/s41534-022-00552-0> (visited on 05/19/2022).
- [9] Johannes Görlitz et al. “Spectroscopic investigations of negatively charged tin-vacancy centres in diamond”. en. In: *New Journal of Physics* 22.1 (Jan. 2020), p. 013048. ISSN: 1367-2630. DOI: 10.1088/1367-2630/ab6631. URL: <https://doi.org/10.1088/1367-2630/ab6631> (visited on 09/14/2021).
- [10] Gilbert Grynberg, Alain Aspect, and Claude Fabre. *Introduction to Quantum Optics*. Cambridge University Press, Sept. 2010. ISBN: 9780521551120.
- [11] Christian Hepp et al. “Electronic Structure of the Silicon Vacancy Color Center in Diamond”. de. In: *Physical Review Letters* 112.3 (Jan. 2014), p. 036405. ISSN: 0031-9007, 1079-7114. DOI: 10.1103/PhysRevLett.112.036405. URL: <https://link.aps.org/doi/10.1103/PhysRevLett.112.036405> (visited on 11/23/2021).
- [12] Takayuki Iwasaki et al. “Tin-Vacancy Quantum Emitters in Diamond”. In: *Physical Review Letters* 119.25 (Dec. 2017), p. 253601. DOI: 10.1103/PhysRevLett.119.253601. URL: <https://link.aps.org/doi/10.1103/PhysRevLett.119.253601> (visited on 09/14/2021).

- [13] Kay D. Jahnke et al. "Electron–phonon processes of the silicon-vacancy centre in diamond". en. In: *New Journal of Physics* 17.4 (Apr. 2015). Publisher: IOP Publishing, p. 043011. ISSN: 1367-2630. DOI: 10.1088/1367-2630/17/4/043011. URL: <https://doi.org/10.1088/1367-2630/17/4/043011> (visited on 05/13/2022).
- [14] A. Javadi et al. "Single-photon non-linear optics with a quantum dot in a waveguide". en. In: *Nature Communications* 6.1 (Oct. 2015), p. 8655. ISSN: 2041-1723. DOI: 10.1038/ncomms9655. URL: <https://www.nature.com/articles/ncomms9655> (visited on 12/15/2021).
- [15] Lukas Novotny. *Lecture Notes on Electromagnetic Fields and Waves*. ETH Zurich, Photonics Laboratory, 2019.
- [16] Nir Rotenberg et al. "Small slot waveguide rings for on-chip quantum optical circuits". EN. In: *Optics Express* 25.5 (Mar. 2017), pp. 5397–5414. ISSN: 1094-4087. DOI: 10.1364/OE.25.005397. URL: <https://www.osapublishing.org/oe/abstract.cfm?uri=oe-25-5-5397> (visited on 11/16/2021).
- [17] Maximilian Ruf et al. "Quantum networks based on color centers in diamond". In: *Journal of Applied Physics* 130.7 (Aug. 2021), p. 070901. ISSN: 0021-8979. DOI: 10.1063/5.0056534. URL: <https://aip-scitation-org.tudelft.idm.oclc.org/doi/10.1063/5.0056534> (visited on 09/13/2021).
- [18] Alison E. Rugar et al. "Narrow-Linewidth Tin-Vacancy Centers in a Diamond Waveguide". In: *ACS Photonics* 7.9 (Sept. 2020), pp. 2356–2361. DOI: 10.1021/acsp Photonics.0c00833. URL: <https://doi.org/10.1021/acsp Photonics.0c00833> (visited on 09/13/2021).
- [19] A. Sipahigil et al. "An integrated diamond nanophotonics platform for quantum-optical networks". In: *Science* 354.6314 (Nov. 2016), pp. 847–850. DOI: 10.1126/science.aah6875. URL: <https://www.science.org/lookup/doi/10.1126/science.aah6875> (visited on 09/15/2021).
- [20] Gergő Thiering and Adam Gali. "Ab Initio Magneto-Optical Spectrum of Group-IV Vacancy Color Centers in Diamond". In: *Physical Review X* 8.2 (June 2018), p. 021063. DOI: 10.1103/PhysRevX.8.021063. URL: <https://link.aps.org/doi/10.1103/PhysRevX.8.021063> (visited on 09/14/2021).
- [21] Henri Thyrrestrup et al. "Quantum Optics with Near-Lifetime-Limited Quantum-Dot Transitions in a Nanophotonic Waveguide". In: *Nano Letters* 18.3 (Mar. 2018), pp. 1801–1806. ISSN: 1530-6984. DOI: 10.1021/acs.nanolett.7b05016. URL: <https://doi.org/10.1021/acs.nanolett.7b05016> (visited on 09/13/2021).
- [22] Matthew E. Trusheim et al. "Transform-Limited Photons From a Coherent Tin-Vacancy Spin in Diamond". In: *Physical Review Letters* 124.2 (Jan. 2020), p. 023602. DOI: 10.1103/PhysRevLett.124.023602. URL: <https://link.aps.org/doi/10.1103/PhysRevLett.124.023602> (visited on 09/13/2021).
- [23] Pierre Türschmann et al. "Coherent nonlinear optics of quantum emitters in nanophotonic waveguides". en. In: *Nanophotonics* 8.10 (Oct. 2019), pp. 1641–1657. ISSN: 2192-8614. DOI: 10.1515/nanoph-2019-0126. URL: <https://www.degruyter.com/document/doi/10.1515/nanoph-2019-0126/html> (visited on 10/05/2021).
- [24] Noel H. Wan et al. "Large-scale integration of artificial atoms in hybrid photonic circuits". en. In: *Nature* 583.7815 (July 2020), pp. 226–231. ISSN: 1476-4687. DOI: 10.1038/s41586-020-2441-3. URL: <https://www.nature.com/articles/s41586-020-2441-3> (visited on 09/13/2021).
- [25] Stephanie Wehner, David Elkouss, and Ronald Hanson. "Quantum internet: A vision for the road ahead". In: *Science* 362.6412 (Oct. 2018), eaam9288. DOI: 10.1126/science.aam9288. URL: <https://www.science.org/lookup/doi/10.1126/science.aam9288> (visited on 09/13/2021).